Inorganic Chemistry

ARTICLE

pubs.acs.org/IC

Theoretical Analysis of the Spin Hamiltonian Parameters in $Co^{(II)}S_4$ Complexes, Using Density Functional Theory and Correlated ab initio Methods

Dimitrios Maganas,[†,§] Silvia Sottini,[‡] Panayotis Kyritsis,[*,†] Edgar J. J. Groenen,[‡] and Frank Neese[*,§]

[†]Inorganic Chemistry Laboratory, Department of Chemistry, National and Kapodistrian University of Athens, GR-15771 Athens, Greece
[‡]Department of Molecular Physics, Huygens Laboratory, Leiden University, P.O. Box 9504, 2300 RA Leiden, The Netherlands
[§]Institute of Theoretical and Physical Chemistry, Wegelerstrasse 12, D-53115 Bonn, Germany

ABSTRACT: A systematic Density Functional Theory (DFT) and multiconfigurational ab initio computational analysis of the Spin Hamiltonian (SH) parameters of tetracoordinate $S = 3/2$ $Co^{(II)}S_4$—containing complexes has been performed. The complexes under study bear either arylthiolato, ArS^-, or dithioimidodiphosphinato, $[R_2P(S)NP(S)R'_2]^-$ ligands. These complexes were chosen because accurate structural and spectroscopic data are available, including extensive Electron Paramagnetic Resonance (EPR)/Electron Nuclear Double Resonance (ENDOR) studies. For comparison purposes, the $[Co(PPh_3)_2Cl_2]$ complex, which was thoroughly studied in the past by High—Field and Frequency EPR and Variable Temperature, Variable Field Magnetic Circular Dichroism (MCD) spectroscopies, was included in the studied set. The magnitude of the computed axial zero-field splitting parameter D (ZFS), of the $Co^{(II)}S_4$ systems, was found to be within ~10% of the experimental values, provided that the property calculation is taken beyond the accuracy obtained with a second-order treatment of the spin—orbit coupling interaction. This is achieved by quasi degenerate perturbation theory (QDPT), in conjunction with complete active space configuration interaction (CAS-CI). The accuracy was increased upon recovering dynamic correlation with multiconfigurational ab initio methods. Specifically, spectroscopy oriented configuration interaction (SORCI), and difference dedicated configuration interaction (DDCI) were employed for the calculation of the **D**-tensor. The sign and magnitude of parameter D was analyzed in the framework of Ligand Field Theory, to reveal the differences in the electronic structures of the investigated $Co^{(II)}S_4$ systems. For the axial complexes, accurate effective $\mathbf{g}'$-tensors were obtained in the QDPT studies. These provide a diagnostic tool for the adopted ground state configuration (±3/2 or ±1/2) and are hence indicative of the sign of D. On the other hand, for the rhombic complexes, the determination of the sign of D required the SH parameters to be derived along suitably constructed symmetry interconversion pathways. This procedure, which introduces a dynamic perspective into the theoretical investigation, helped to shed some light on unresolved issues of the corresponding experimental studies. The metal hyperfine and ligand super-hyperfine **A**-tensors of the C_2 $[Co\{(SPPh_2)(SP^iPr_2)N\}_2]$ complex were estimated by DFT calculations. The theoretical data were shown to be in good agreement with the available experimental data. Decomposition of the metal **A**-tensor into individual contributions revealed that, despite the large ZFS, the observed significant anisotropy should be largely attributed to spin—dipolar contributions. The analysis of both, metal and ligand **A**-tensors, is consistent with a highly covalent character of the Co—S bonds.

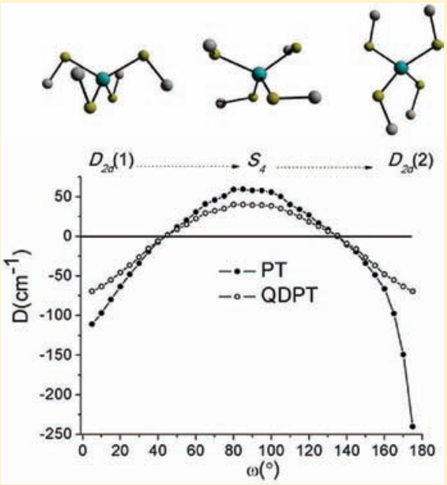

INTRODUCTION

Extensive studies over the past two decades have revealed a close interdependence of the structural, electronic, and functional properties of the active site of metalloproteins.[1] During this period, there has been significant progress in the development of both physicochemical and theoretical methods.[2] The application of these methods has made it possible to analyze the electronic structures of the active sites of metalloproteins with increasing sophistication. For such biological metal sites, as well as for their chemical analogues, elucidating the contribution of electronic structures to reactivity[3] is an active field of multi-disciplinary research.[4,5]

A large proportion of metalloenzymes contain paramagnetic active sites, which are involved, for instance, in electron transport or redox catalysis. The method of choice for probing the electronic structure of such systems is Electron Paramagnetic Resonance (EPR) spectroscopy.[6] During the past decade, the application of higher frequencies and magnetic fields has made it possible to investigate an increasing number of $S > 1/2$ systems, especially those of "integer spin", which were traditionally considered to be "EPR silent".[7,8] One of the reasons for

Received: February 11, 2011
Published: August 17, 2011

rendering such systems inaccessible to conventional X-band EPR spectrometers is the large axial component (D) of their zero-field splitting (ZFS).[9] The magnitude and the sign of D, and the remaining Spin Hamiltonian (SH) parameters ($\mathbf{g}$, metal hyperfine and ligand super-hyperfine $\mathbf{A}$-tensors), reveal crucial information on the electronic structure descriptors of the paramagnetic system.[2]

One of the important goals of this research is to clarify the underlying magnetostructural correlations that control the magnitude and the sign of D.[10,11] This is also important for the design of materials with tailored magnetic properties, such as Single Molecule Magnets (SMMs). In the latter case, the most important parameter is the magnetic anisotropy, expressed via the D parameter.[12−15] Suitable methods for probing the ZFS experimentally include magnetic susceptibility measurements and Magnetic Circular Dichroism (MCD) spectroscopy.[9,16,17] However, both approaches involve thermal depopulation experiments and hence suffer from limited accuracy. The same restriction applies to conventional X-band EPR spectroscopy, in which variable temperature measurements are necessary to extract ZFS values.[18] In addition, the magnetic susceptibility and magnetization measurements are influenced by the presence of contaminating species. These limitations are to some extent overcome by applying High-Field and Frequency EPR methods (HF-EPR), because in this case the ZFS is directly determined.[19] Thus, HF-EPR has become the most reliable method for accurate ZFS determinations.[8,20] In addition to HF-EPR methods, ZFS parameters can also be directly determined by far-IR magnetic spectroscopy,[21−23] as well as by Frequency Domain Fourier Transform (FD-FT) THz-EPR spectroscopy.[24]

Focusing on the EPR properties of $\mathrm{Co^{(II)}}$ coordination compounds, we note that there is an extensive relevant literature on simple complexes,[17,18,25] (and references therein), as well as on $\mathrm{Co^{(II)}}$-containing proteins or enzymes. With respect to the latter, the $3d^7$ $\mathrm{Co^{(II)}}$ ion is used as a spectroscopic and paramagnetic probe, replacing either paramagnetic[26] or, most commonly, diamagnetic bio-metals like $\mathrm{Zn^{(II)}}$.[27] The biological $\mathrm{Co^{(II)}}$ sites and the corresponding chemical analogues, which have been under investigation, include single and binuclear systems. The latter have been extensively studied by MCD spectroscopy.[28−30]

The first $\mathrm{Co^{(II)}}$ complex that was thoroughly studied by HF-EPR was the pseudo-tetrahedral $[\mathrm{Co(PPh_3)_2Cl_2}]$ complex.[17] In the same work, variable temperature, variable field (VTVH) MCD studies were also employed, with the ZFS determined by the two methods being in very good agreement. Motivated by these seminal studies, we have recently extended the data set of reliably determined EPR parameters of $\mathrm{Co^{(II)}}$ systems, by studying the $[\mathrm{Co\{(SPPh_2)_2N\}_2}]$[31] and $[\mathrm{Co\{(SPPh_2)(SP^iPr_2)N\}_2}]$[32] complexes, which contain the deprotonated form, $\mathrm{L^-}$, of the dithioimidodiphosphinato ligands, $\mathrm{LH = R_2P(S)NHP(S)R'_2}$, R, R′ = Ph or ^{i}Pr.[33−36] In the following, the above type of $\mathrm{CoS_4}$-containing complexes will be denoted as $\mathrm{Co^{R,R'}L_2}$.The experimental investigations aimed at correlating the electronic properties of $\mathrm{Co^{(II)}S_4}$-containing complexes, derived by HF-EPR[18] and Electron Nuclear Double Resonance (ENDOR)[37] experiments, with their structural properties. Very recently, a series of four-coordinate $\mathrm{Co^{(II)}}$ complexes, containing the hydro(tris-pyrazol-1-yl)borate ("scorpionate") anion as ligand, have been studied by HF-EPR spectroscopy.[25]

Previously, Hirota and co-workers studied the magnetic and X-band EPR properties of anionic $\mathrm{Co^{(II)}S_4}$-containing complexes, namely, $\mathrm{A_2[Co^{(II)}(SPh)_4]}$, A = $\mathrm{Me_4N}$, $\mathrm{Et_4N}$, $\mathrm{Ph_4P}$, as well as $\mathrm{(Et_4N)_2[Co(SR)_4]}$, R = $\mathrm{C_6H_4}$-p-Me, $\mathrm{C_6H_5}$-p-Cl, $\mathrm{C_6F_5}$, bearing arylthiolates as ligands.[38−40] In particular, the different symmetries of the $\mathrm{(PPh_4)_2[Co^{(II)}(SPh)_4]}$[39] and $\mathrm{(Me_4N)_2[Co^{(II)}(SPh)_4]}$[40] complexes ($D_{2d}$ and S_4, respectively) because of countercation effects were correlated with remarkably different sets of EPR parameters, including rather large (up to 100 $\mathrm{cm^{-1}}$) ZFS values.[38−40] In addition, a D-value of 30 $\mathrm{cm^{-1}}$ was recently reported by Haase and co-workers for a thiourea-containing $\mathrm{Co^{(II)}S_4}$ complex, based on magnetic susceptibility, magnetization, and MCD studies.[16]

The theoretical prediction of EPR parameters has made significant progress in the past few years.[41] The relevant microscopic relativistic terms that enter in the calculation of the ZFS are the direct magnetic dipole−dipole interaction (spin−spin coupling, SSC) and the spin−orbit coupling (SOC). The SSC contributes to the ZFS in first order of perturbation theory (PT) and, therefore, can be calculated as an expectation value. The SOC contribution, however, arises in second order and, hence, is related to a complete sum over states which contain contributions from excited states of spin multiplicities different from the ground state. For octahedral complexes of $\mathrm{Cr^{(III)}}$,[42] $\mathrm{Mn^{(II)}}$,[10] and $\mathrm{Mn^{(III)}}$,[43] the SSC term, as well as spin flip excitations, have been shown to be crucial for the successful computational estimation of ZFS values. However, as shown by theoretical calculations of their MCD spectra, the ZFS of tetrahedral, $S = 3/2$, $\mathrm{Co^{(II)}}$ complexes is strongly dominated by the SOC interaction.[44] In fact, owing to the near orbital degeneracy, the SOC in such systems can be rather strong, leading to very large reported D values (up to ∼100 $\mathrm{cm^{-1}}$).[38] Such values would be well outside the ZFS range experimentally accessible by EPR spectroscopy, including HF-EPR methods, the upper limit of which is currently around 25 $\mathrm{cm^{-1}}$.[25] The experimental consequence of very large ZFS values is that only transitions within the lowest Kramers doublet (in the low Zeeman field limit) can be observed.[45] For such systems, low-order perturbation theoretical methods are not expected to yield accurate predictions. This is particularly relevant for modern theories probing electronic structures, since property calculations are usually based upon linear response theory, which is equivalent to an infinite sum over states in second-order PT.[46] In addition to the axial component, D, of the ZFS, environments of low symmetry are characterized by a non-zero rhombic ZFS component E. In the limit of extreme rhombicity ($E/D = 1/3$), the sign of D becomes ambiguous.[47]

Up until very recently, the literature was lacking reliably determined experimental SH parameters for $\mathrm{Co^{(II)}S_4}$-containing systems. The recent availability of precise experimental SH parameters for $\mathrm{Co^{Ph,Ph}L_2}$ and $\mathrm{Co^{Ph,^iPr}L_2}$,[18,37] led us to apply multi-reference ab initio methods to these, as well as the $\mathrm{Co^{(II)}S_4}$-containing complexes reported by Hirota and co-workers.[38−40] Hence, in this work, the corresponding complete set of SH parameters are calculated with the aid of DFT and correlated ab initio methods. The results help to clarify controversial matters which were not resolved by the experimental investigations, for example, the sign of D in highly rhombic systems,[18] and provide further insight into the magnetostructural correlations that are operative in pseudo-tetrahedral $\mathrm{Co^{(II)}S_4}$-containing complexes.

■ THEORY

General Information. The phenomenological description of the EPR spectra of the high spin, $S = 3/2$ $\mathrm{Co^{(II)}}$ complexes, is based upon the SH that includes the ZFS, the electron Zeeman interaction, the cobalt hyperfine, and the nuclear Zeeman interaction:

$$\hat{H}_{spin} = \hat{S}\mathbf{D}\hat{S} + \beta_e \mathbf{B}\mathbf{g}\hat{S} + \hat{S}\mathbf{A}^{(\mathrm{Co})}\hat{I} + \beta_N \mathbf{B}\mathbf{g}_N^{(Co)}\hat{I} \tag{1}$$

$\hat{S}$ and $\hat{I}$ represent the electron-spin and cobalt nuclear-spin angular momentum operators, the **D**, **g**, and $\mathbf{A}^{(\mathbf{Co})}$ tensors represent the ZFS, the Zeeman interaction, and the metal hyperfine interaction, respectively, while β_e and β_N are the corresponding Bohr magnetons and **B** is the magnetic flux density. A full analytical solution of the SH eigenvalue problem for the $S = 3/2$ case can be found in textbooks.[48] It should be noted that the low symmetry of the Co$^{(II)}$ complexes under study precludes the assumption that the principal axes of **D** and **g** are parallel. The first term in eq 1 gives rise to four magnetic sublevels, which consist of two Kramers doublets,

$$|0^{\pm}\rangle = \cos\theta \left|\frac{3}{2}, \pm\frac{3}{2}\right> + \sin\theta \left|\frac{3}{2}, \mp\frac{1}{2}\right> \tag{2}$$

$$|1^{\pm}\rangle = \cos\theta \left|\frac{3}{2}, \pm\frac{1}{2}\right> - \sin\theta \left|\frac{3}{2}, \mp\frac{3}{2}\right> \tag{3}$$

where the angle θ, in terms of the ZFS parameters, is given by

$$\tan(2\theta) = \sqrt{3}\frac{E}{D} \tag{4}$$

The energy separation between the doublets amounts to $2D'$, with D' being equal to $(D^2 + 3E^2)^{1/2}$. The ZFS parameters are defined in terms of the principal values of the **D**-tensor, by $D = {}^3/_2 D_{zz}$ and $E = {}^1/_2(D_{xx} - D_{yy})$, in a coordinate system that diagonalizes **D**. Although M_S is not a good quantum number, we will refer to the $|1^{\pm}\rangle$ and $|0^{\pm}\rangle$ doublets as $\pm 1/2$ and $\pm 3/2$, respectively.

Spin–Orbit Coupling (SOC). The most important step in modeling optical and magnetic phenomena of transition metal ions is a realistic treatment of SOC. The effect of SOC is that it mixes states of different spin multiplicities (with $\Delta S = 0, \pm 1$) and splits the different M_s members of a given total S multiplet. The effect may occur in first order PT for the orbitally degenerate states, but it occurs in second order for all states with $S > 1/2$. As such, the SOC reintroduces some orbital angular momentum into the wave function, even if it is "quenched" by low-symmetry.

Quasi-Degenerate PT. In quasi-degenerate PT, one starts by obtaining an approximate solution of the Born–Oppenheimer (BO) Hamiltonian of a multireference type, such as CASSCF, MRCI, or multireference in the form of $|\Psi_I^{SS}\rangle = \Sigma_\mu C_{\mu I}|\Phi_\mu^{SS}\rangle$. Here, the upper indices SS stand for a many-particle wave function with spin quantum number S and spin projection quantum number M_s=S. Since the BO Hamiltonian does not contain any complex valued operator, the $|\Psi_I^{SS}\rangle$ solutions may be chosen to be real-valued. Introduction of SOC requires the lifting of the $(2S + 1)$ degeneracy of the total spin S $\hat{H}_{BO}$ eigenfunctions. Thus, the basis of the treatment are the $|\Psi_I^{SM}\rangle$ states, in which I covers all the roots calculated in the first step of the procedure and $M = -S, ..., S$ enumerates all members of a given multiplet. Matrix elements over the $|\Psi_I^{SM}\rangle$ functions are readily generated using the Wigner–Eckart theorem, since all $(2S + 1)$ members of the multiplet share the same spatial part of the wave function.[49]

On the basis of the above functions, SOC and SSC effects, along with the Zeeman interaction, can be included by means of quasi-degenerate perturbation theory (QDPT), which amounts to the diagonalization of the matrix representation of $\hat{H}_{BO}$ + $\hat{H}_{SOC}$ + $\hat{H}_{SSC}$ + $\hat{H}_Z$, in the basis of the states $|\Psi_I^{SM}\rangle$:

$$\begin{aligned} &\langle \Psi_I^{SM}|\hat{H}_{BO} + \hat{H}_{SOC} + \hat{H}_{SSC} + \hat{H}_Z|\Psi_J^{S'M'}\rangle \\ &\quad = \delta_{IJ}\delta_{SS'}\delta_{MM'}E_I^{(S)} + \langle \Psi_I^{SM}|\hat{H}_{SOC} + \hat{H}_{SSC} \\ &\qquad + \hat{H}_Z|\Psi_J^{S'M'}\rangle \end{aligned} \tag{5}$$

Diagonalization of this matrix yields the energy levels and eigenvectors of the coupled states$\{\Psi_I^{SM}\}$. This procedure yields the **D** and **g** tensors directly. Alternatively, the SOC components of D are calculated through well-established second order PT equations:[50]

$$\begin{aligned} D_{kl}^{SOC-(0)} = &-\frac{1}{S^2}\sum_{b(S_b=S)} \Delta_b^{-1}\langle 0SS|\sum_i z_{k;i}^{SOMF}\hat{s}_{i;z}|bSS\rangle \\ &\langle bSS|\sum_i z_{l;i}^{SOMF}\hat{s}_{i;z}|0SS\rangle \end{aligned} \tag{6}$$

$$\begin{aligned} D_{kl}^{SOC-(-1)} = &-\frac{1}{2S(S-1)}\sum_{b(S_b=S-1)} \Delta_b^{-1} \\ &\langle 0SS|\sum_i z_{k;i}^{SOMF}\hat{s}_{i;+1}|b(S-1)(S-1)\rangle \\ &\langle b(S-1)(S-1)|\sum_i z_{l;i}^{SOMF}\hat{s}_{i;-1}|0SS\rangle \end{aligned} \tag{7}$$

$$\begin{aligned} D_{kl}^{SOC-(+1)} = &-\frac{1}{(S+1)(2S+1)}\sum_{b(S_b=S+1)} \Delta_b^{-1} \\ &\langle 0SS|\sum_i z_{k;i}^{SOMF}\hat{s}_{i;-1}|b(S+1)(S+1)\rangle \\ &\langle b(S+1)(S+1)|\sum_i z_{l;i}^{SOMF}\hat{s}_{i;+1}|0SS\rangle \end{aligned} \tag{8}$$

where the first term describes contributions from excited states of the same spin as the ground state ($S' = S$), the second term arises from states with $S' = S - 1$, and finally the third term arises from states with $S' = S + 1$. Here, k and l denote Cartesian components x, y, and z, and Δ_b is the energy difference between the ground state and the b^{th} excited state in the absence of the SOC interaction. Here and throughout the paper, the SOC has been represented by the spin–orbit mean-field (SOMF) method, in the implementation already described.[51] In this approach, the SOC appears as an effective one-electron operator of the form $\hat{H}_{SOMF} = \Sigma_i \mathbf{z}_i^{SOMF}\mathbf{s}_i$.

g-Values. For a system with an odd number of electrons, the doubly degenerate eigenvalues obtained from the QDPT procedure represent Kramers pairs, which are used to build the matrix elements of the total spin operator and the total angular momentum operator of the Zeeman Hamiltonian term. By denoting Ψ as a solution and $\overline{\Psi}$as its Kramers partner, the eigenvalues Φ are given by the matrix elements notation as:

$$\Phi_{11}^k = \langle \Psi|\hat{L}_k + g_e\hat{S}_k|\Psi\rangle, \quad \Phi_{12}^k = \langle \Psi|\hat{L}_k + g_e\hat{S}_k|\overline{\Psi}\rangle, \quad k = x, y, z \tag{9}$$

The elements of the g-matrix are then obtained as:

$$\begin{aligned} g_{kz} = 2c\Phi_{11}^k, \quad g_{ky} = -2c\mathrm{Im}(\Phi_{12}^k), \quad g_{kx} \\ = -2c\mathrm{Re}(\Phi_{12}^k) \end{aligned} \tag{10}$$

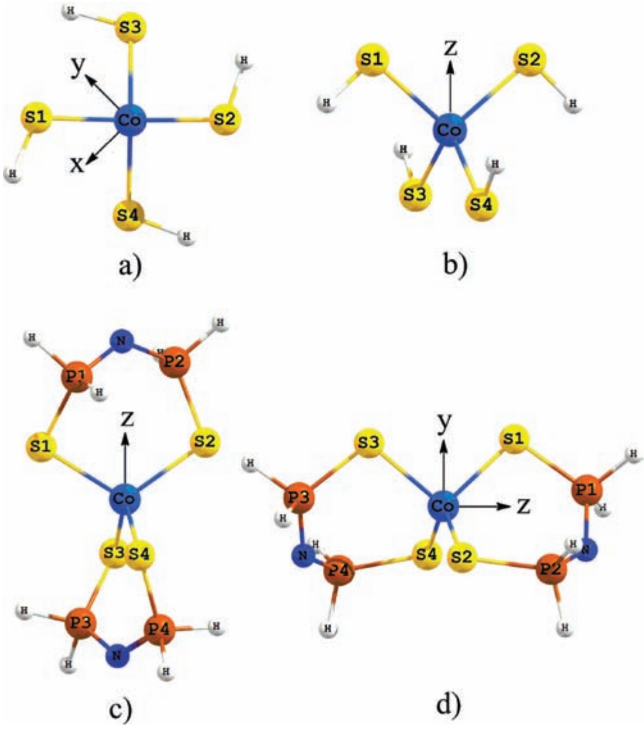

Figure 1. ^{H}**1** (a), ^{H}**2** (b), ^{H}**3** (c), and ^{H}**4** (d) models. For **1**, **2** and **3**, **4**, a unified reference coordinate system was chosen, according to the experimental data of the effective **g** tensors. For **2** and **3**, g'_z and consequently D_{zz}, is parallel to the principal symmetry axis (since $E/D{\sim}0$), whereas for **1** and **4**, g'_z and g'_y are parallel to the principal symmetry axis, respectively ($E/D{\sim}1/3$).

Then the true **G** tensor can be built from the *g*-matrices as

$$G = gg^T \tag{11}$$

Further, diagonalization of **G** yields positive eigenvalues, the square root of which give the principal values of the g-matrix:[52]

$$g_{xx} = \sqrt{G_{xx}}, \quad g_{yy} = \sqrt{G_{yy}}, \quad g_{zz} = \sqrt{G_{zz}} \tag{12}$$

Hyperfine Coupling Term (HFC). In the language of analytic derivative theory, the HFC term is defined as the second mixed derivative of the total ground state energy with respect to the electron spin $\hat{S}$ as well as to the nuclear spin $\hat{I}$ by eq 13

$$A_{\mu\nu} = \frac{\partial^2 E}{\partial \hat{S}_\mu \partial \hat{I}_\nu^{(A)}} \tag{13}$$

The hyperfine coupling tensor of a nucleus consists of three contributions, which are the isotropic Fermi contact (FC), the anisotropic spin−dipolar contributions (SD) (both of first order in PT), and the SOC contribution (of second order in PT).

$$A^A_{\mu\nu} = A^{A;c}_{\mu\nu} + A^{A;d}_{\mu\nu} + A^{A;SO}_{\mu\nu} \tag{14}$$

The three contributions to the HFC are explicitly given below:

(a) The isotropic Fermi contact term (FC), arising from the finite spin density on the nucleus under investigation, which for the *N*-th nucleus is calculated as

$$a_{iso}(N) = \left(\frac{4}{3}\pi\langle S_z\rangle^{-1}\right) g_e g_N \beta_e \beta_N \rho(\vec{R}_N) \tag{15}$$

where $\langle S_z\rangle$ is the expectation value of the *z*-component of the total spin, g_e, g_N are the spin and nuclear g-factors, β_e and β_N are the corresponding Bohr magnetons, $\rho(\vec{R}_N)$ is the spin density at the nucleus, and $g_e g_N \beta_e \beta_N \equiv P_N$ refers to a commonly used proportionality factor with units of $MHz \times \text{bohr}^3$.[53]

(b) The spin dipole part (SD) arises from the magnetic dipole interaction of the magnetic nucleus with the magnetic moment of the electron, and it is calculated as an expectation value over the spin density as

$$A^{dip}_{\mu\nu}(N) = P_N \sum_{kl} \rho_{kl} \langle \varphi_k | r_N^{-5}(3\vec{r}_{N\mu}\vec{r}_{N\nu} - \delta_{\mu\nu} r_N^2) | \varphi_l \rangle \tag{16}$$

Here, ρ is the spin density matrix and $\vec{r}_N$ is a vector of magnitude r_N that points from the nucleus in question to the electron. Finally, $\{\phi\}$ is the set of the chosen basis functions.

(c) The second order contribution arising from SOC is given by

$$A^{orb}_{\mu\nu}(N) = -\frac{1}{2S} P_N \sum_{kl} \frac{\partial \rho_{kl}}{\partial I_\mu} \langle \phi_k | h_\nu^{SOC} | \phi_l \rangle \tag{17}$$

The derivative of the spin density is computed by solving the coupled-perturbed SCF equations with respect to the nucleus-orbit coupling as perturbation. The nucleus-orbit coupling is represented by the operator:

$$h_\nu^{SOC}(N) = \sum_i r_{iA}^{-3} l_{i,\nu}^{(A)} \tag{18}$$

■ COMPUTATIONAL DETAILS

All calculations were performed with the ORCA computational package.[54] For the DFT calculations, the structures of the complexes $[Co(SPh)_4]^{2-}$ (S_4) (**1**),[40] $[Co(SPh)_4]^{2-}$ (D_{2d}) (**2**) (vide infra), $Co^{Ph,Ph}L_2$ (**3**),[31] and $Co^{Ph,iPr}L_2$ (**4**)[32] were studied using the BP86[55,56] and B3LYP[55,57,58] functionals for geometries/frequencies and spectroscopic properties, respectively. The Ahlrichs polarized triple-ζ(TZVP) quality[59a] basis set was used for all atoms, in combination with the TZV/J Coulomb fitting basis for the resolution of identity (RI) approximation (in BP86 calculations). For geometry optimizations, a one-center relativistic correction is applied by employing the implemented standard second-order Douglas−Kroll−Hess (DKH) procedure.[60−62] In addition, for the anionic complexes **1** and **2**, one set of diffuse s, p functions (taken from 6-311++G(2d, 2p) basis set)[59b] were added to the ligand atoms. Where available, the coordinates were taken from the crystal structures. To make the ab initio calculations feasible, the bulky Ph or ^{i}Pr groups of the studied complexes were replaced by H or Me.[63] This leads to the corresponding model complexes, denoted as ^{H}**1**, ^{Me}**1**, ^{H}**2**, ^{H}**3**, and ^{H}**4** (Figure 1). For all atoms the TZVP basis set was used, whereas for the Co center the TZVPP[59] was employed. The higher accuracy basis set def2-TZVP(-f)[64] was also tested, and found to give similar results as the TZVP/TZVPP combination. The ab initio calculations, were carried out in the basis of all 10 roots for the quartet states (arising from the ^{4}F and ^{4}P terms of Co^{2+}) together with 35 doublet roots (arising from the ^{2}G, ^{2}H, ^{2}P, ^{2}D, and ^{2}F terms of Co^{2+}). MR-difference dedicated CI with two degrees of freedom (DDCI2) and Spectroscopy ORiented CI (SORCI)[65] calculations were performed on top of the state averaged complete active space self-consistent field (SA-CASSCF) reference wave functions, to recover the

Table 1. Experimental and BP86/TZVP/DKH-Optimized Co−S_i Bond Lengths (Å) and S_i−Co−S_i Angles (deg)

complexes	bond	experiment	optimized	Meyer bond orders
1	Co−S_i	2.302(3)	2.283	0.79
	S_1−Co−S_2	117.1(1)	119.6	
2	Co−S_i	2.303(4)[89]	2.296	0.79
	S_1−Co−S_2	96.6(3)[89]	95.2	
3	Co−S_i	2.311(2)	2.298	0.79
	S_1−Co−S_2	113.2(3)	110.4	
4	Co−S_{13}(P_{13})[a]	2.336(3)	2.314	0.77
	Co−S_{24}(P_{24})[b]	2.301(3)	2.283	0.82
	S_1−Co−S_3	95.8(2)	97.5	
	S_2−Co−S_4	110.7(2)	114.5	

[a] $P_{13} \equiv$ P(Ph). In ref 37 P_{13} is referred as P_{12}. [b] $P_{24} \equiv$ P(^{i}Pr). In ref 37 P_{24} is referred as P_{34}.

Scheme 1. Symmetry Definition of the $Co^{II}(SR)_4$ Core As a Function of the Torsion Angles ω_i[a]

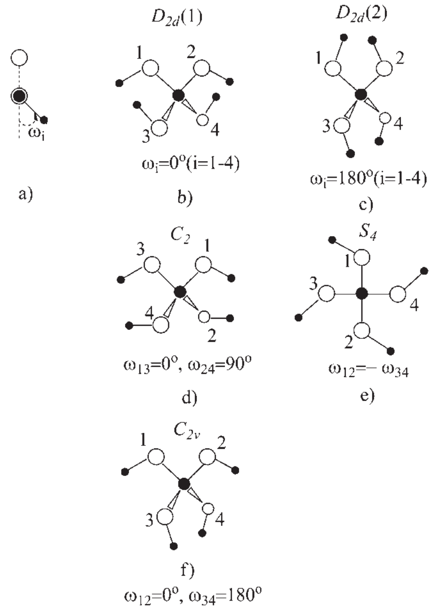

[a] (a) Definition of the torsion angle ω_i, for the rotation of residue R_i around the Co−S_i axis. (b) $D_{2d}(1)$ and (c) $D_{2d}(2)$ conformations, labels (1) and (2) indicate that ω_i is 0° and 180°, respectively. (d) An ideal C_2 conformation, $\omega_{13} = 0°$, $\omega_{24} = 90°$. (e) The S_4 conformation, $\omega_{12} = -\omega_{34}$. (f) A C_{2v} conformation, $\omega_{12} = 0°$, $\omega_{34} = 180°$. In all sketches: Co = large filled circles, R = small filled circles, S = open circles.

major part of the differential dynamic correlation between the ground and the excited states. The minimal active space was chosen to consist of 7 electrons in the 5 d-orbitals (CAS(7,5)). As explained previously,[44] we have used individual selection in the SORCI calculations, to decrease the computational burden. The relevant thresholds are $T_{\text{sel}} = 10^{-6}$ Eh and $T_{\text{pre}} = 10^{-5}$. The B3LYP/def2-TZVP coupled-perturbed (CP) method is used for the calculation of the ZFS values, which uses revised prefactors for the spin-flip terms and solves a set of coupled-perturbed equations for the SOC perturbation, as already described in detail.[66] The D^{ss} part that accounts for the SSC contribution to the ZFS, is treated with the "UNO" option. This allows the calculation of the SSC term, with a restricted spin density obtained from the singly occupied unrestricted natural orbitals. The objective for this procedure is discussed in ref 66. The calculation of the eigenvalues of the diagonalized 4 × 4 ZFS matrix shows that the energy separation between the two Kramers doublets amounts to $2D'$, where $D' = (D^2 + 3E^2)^{1/2}$. The energy difference between the analytic eigenvalues can be matched with the one obtained from the QDPT procedure, to obtain values for D and E. In fact, if the E/D ratio is defined via second-order perturbation theory, the D value can be extracted from the calculated QDPT energy separation between the $|\pm 1/2\rangle$ and $|\pm 3/2\rangle$ Kramers doublets.

For the quantum chemical construction of the interconversion pathways, we have initially constructed the DFT BP86/TZVP relaxed scanned potential energy surfaces for the quartet states, along the torsion angle ω_i, followed by state averaged CASSCF(7,5) (SA-CASSCF) calculations at the BP86 optimized structures.

Hyperfine structure calculations were performed using DFT methods. The ^{59}Co hyperfine and ^{31}P super-hyperfine coupling constants (HFCs) were obtained by performing additional single point calculations, on the model $^{\text{H}}$**4** geometry. The isotropic HFC A_{iso} and the traceless anisotropic dipolar A_i were calculated directly as the expectation values of the appropriate operators over the spin density. Furthermore, the spin−orbit contribution to the hyperfine interaction was also calculated.[67] The hyperfine structure calculations were performed by employing GGA: BP86 and PBE0,[68] hybrid-GGA: B3LYP, meta-GGA: TPSS,[69] TPSSh,[70] TPSS0[71] and the double hybrid (DHDF): B2PLYP[72] density functional. The accuracy of these functionals was assessed in ref 73. The CP(PPP)[74] basis set was used for the metal center. For the remaining atoms, the TZVP basis set was used. In addition, for the metal center, the isotropic and dipolar hyperfine coupling contributions were relativistically corrected, by applying the zero-order regular approximation (ZORA).[75−77]

RESULTS AND DISCUSSION

Structural Considerations. Among the complexes studied in this work, X-ray crystallographic structures are available for **1**,[40] **3**,[31] and **4**.[32] Since there are no structural data available for **2**, the computed data for **2** were compared to those of the available analogue $[Co(S^{tpdp}Ph)_4]^{2-}$ (D_{2d}) bearing the *N*-(2-thiophenyl)-2,5-dimethylpyrrole(H-tpdp) ligand, reported by Krebs and coworkers.[78] The calculated Co−S distances and S−Co−S angles (Table 1), based on the optimized structures **1**−**4**, are in close agreement with the experimental ones (within ~0.03 Å and 1−4°, respectively). The problem of probing the electronic properties of a four-coordinate $Co^{(II)}$ complex can be treated in terms of geometric transformations between three basic, idealized $Co^{(II)}(SR)_4$ geometries, R = C or P with D_{2d}, S_4, and C_2 symmetries (Scheme 1). The distortions from the T_d symmetry are an intrinsic property of the $M^{(II)}(SR)_4$ centers and can be quantified by the torsion angles ω_i (R−S−Co−S), (Scheme 1).[79,80] In particular, for stereochemical reasons,[38] the $[M^{(II)}(SPh)_4]$ moieties may only exhibit $D_{2d}(1)$ or S_4 symmetries, which requires the torsion angle relationships $\omega_i = 0°$ and $\omega_{13} = -\omega_{24}$ to hold. On the other hand, the possible torsion angles ω_i are restricted by the dithioimidodiphosphinato ligands L. In the ideal case, only two conformations are expected for high spin $Co^{R,R'}L_2$ complexes: those of $D_{2d}(2)$ and C_2 symmetries, which require the torsion angle relationships $\omega_i = 180°$ and $\omega_{13} = 0°$, $\omega_{24} = 90°$, respectively, to hold. Hence, complexes **1** and **2** exhibit S_4 and $D_{2d}(1)$ symmetries, whereas **3** and **4** exhibit $D_{2d}(2)$ and C_2 symmetries, respectively.The geometry of $[Co(PPh_3)_2Cl_2]$[17] approximates the C_{2v} symmetry and therefore this complex can be included in the same unified representation scheme (Scheme 1).

Electronic Structures. In ideal T_d geometry, the tetracoordinate $Co^{(II)}$ complexes possess a $^4A_2$ ground state, with a half-filled t_2 subshell $e^4t_2^3$. The important single excitations within the

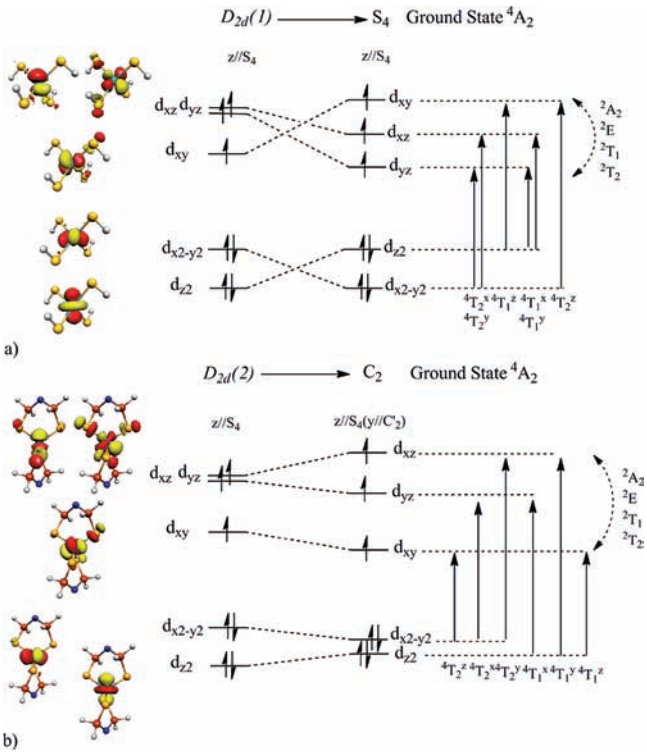

Figure 2. Metal d-based MOs and term symbols (analyzed under approximate T_d symmetry), arising from single excitations in (a) $^{\mathrm{H\ or\ Me}}$**1** and $^{\mathrm{H\ or\ Me}}$**2** and (b) $^{\mathrm{H}}$**3** and $^{\mathrm{H}}$**4**. The indicated orbital occupation pattern refers to the $^4A_2$ ground state.

metal d-shell are those from the doubly occupied e (d_{z^2} and $d_{x^2-y^2}$)-MOs to the singly occupied t_2 (d_{xy}, d_{xz}, and d_{yz})-set. These excitations give rise to two quartet excited states ($^4T_1$ and $^4T_2$). Since in T_d symmetry only the T_2 excited states can couple with the A_2 ground state via SOC,[53] in the following analysis only the lowest energy $^2T_2$ excited state, which represents intra-SOMO spin-flip transitions, is taken into account. The other $^2T_2$ excited states (essentially excitations to $e^3t_2^4$ coupled to a spin-flip) are shown to contribute negligibly (~0.01%). Therefore they were excluded from the present analysis (vide infra). Under conditions favoring further symmetry lowering, there will be further splitting of the x, y, z components of the T_2 states, such that $T_2^x \equiv E^x$, $T_2^y \equiv E^y$, $T_2^z \equiv B^z$ in D_{2d} and S_4 symmetries (and/or $T_2^x \equiv E^x$, $T_2^y \equiv E^y$, $T_2^z \equiv A^z$ in $\sim C_{2v}$ symmetry). In agreement with expectations from Ligand Field Theory (LFT) for D_{2d}, S_4, and C_2 symmetries, the model complexes exhibit the $d_{z^2}^{\,2}d_{x^2-y^2}^{\,2}d_{xy}^{\,1}d_{xz}^{\,1}d_{yz}^{\,1}$ (D_{2d}, complexes **2** and **3**), $d_{x^2-y^2}^{\,2}d_{z^2}^{\,2}d_{xz}^{\,1}d_{yz}^{\,1}d_{xy}^{\,1}$($S_4$, complex **1**), and $d_{z^2}^{\,2}d_{x^2-y^2}^{\,2}d_{xy}^{\,1}d_{xz}^{\,1}d_{yz}^{\,1}$ (C_2, complex **4**) electron configurations, as illustrated in Figure 2.

EPR Spectroscopy. The ZFS parameters of complex **1** have been reported as $D = \sim 6.2$ cm^{-1} and $E/D = |0.3|$.[38,40] Fukui et al. described the symmetry of this complex as approximately S_4, which seems to be at variance with the rhombicity of the ZFS. The conclusion, as regards the positive sign of D, is based on the analysis of the principal effective g' values. However, this analysis cannot be conclusive because the value of E/D is close to 1/3. The principal g' values determined experimentally for this complex are 1.64, 2.34, and 5.68. A similar behavior has been observed experimentally for complex **4** (1.62, 2.38, and 6.44), the magnitude of D for which, however, is larger ($|D| = 14.1$ cm^{-1}).[18] In both cases, the observed extreme rhombicity reflects principal g' values compatible with both negative and positive D, and, consequently, the order of the Kramers doublets is left undetermined by the experiment.

For complex **2**, the ZFS parameters were determined by a combination of EPR and magnetic susceptibility measurements and found to be $D = -70 \pm 10$ cm^{-1} and $E/D < |0.09|$.[38−40] The effective g-values were reported as <0.6, <1.5, and 7.75 ± 0.1. Only upper limits of the lowest g' values could be determined, because the EPR experiments were limited to X-band frequency and magnetic fields below 1 T. For complex **3**, a system of approximately S_4 symmetry, the effective g' values (0.3, 0.3, and 7.12) are very similar to those of complex **2**, while the D-value is also negative but much smaller ($D = -11.9 \pm 0.2$ cm^{-1}).[18]

For complexes **3** and **4**, the Kramers doublets are about 24 and 30 cm^{-1} apart ($2D'$). An accurate value of this splitting, derived from HF-EPR and VTVH-MCD studies, has also been reported for $[Co(PPh_3)_2Cl_2]$, which is of comparable size (29 cm^{-1}).[17] For the latter complex, it was recently shown, in the context of MCD spectroscopy, that accurate ZFS predictions can be obtained by multireference ab initio calculations.[44]

Nature of the SH Parameters. Qualitative insight into the nature of the SH parameters is provided by an LFT type of approach, described by equations presented explicitly elsewhere.[53] Despite the fact that these equations are too simplistic, they provide insight into the nature of the SH parameters. In fact, they demonstrate the importance of an accurate estimation of the SOC contribution in the prediction of the **D**, **g**, and HFC **A** tensors. The magnitude of the SOC term crucially depends on the energies of the most important d−d excited states, involving spin-conserving, as well as intra-SOMO spin-flip, transitions. In addition, an accurately determined SOC contribution can only be achieved if the metal-ligand bond covalencies are properly described and low-symmetry effects are accurately taken care off.

Quantitatively, the LFT approach has been remarkably successful in interpreting the magnetic properties of coordination compounds of many metal ions, such as $Fe^{(IV)}$,[81,82] $Co^{(II)}$,[44] and $V^{(III)}$.[83] However, it should be emphasized, that for quantitative purposes, these equations should be applied with care, since they are restricted in the regime in which PT is valid, which is not always the case, as it will be shown in the following sections. Toward this target, in an effort to treat such a problem in a more general and elaborate way, DFT and multiconfigurational ab initio methods have been employed for the calculation of the SH parameters of high spin $Co^{(II)}S_4$-containing complexes.

D-Tensor. To a first approximation, quantitative predictions of the **D**-tensor of the truncated models $^{\mathrm{Me}}$**1**, $^{\mathrm{H}}$**2**, $^{\mathrm{H}}$**3**, and $^{\mathrm{H}}$**4** were performed, by applying linear response DFT theory.[66] The results, presented in Table 2, are, unfortunately, in poor agreement with the experimental data, irrespective of whether the completely optimized or the constrained geometries of the respective experimental structures were used as the structural basis of the calculations. The predicted magnitude of D strongly depends on the employed structure, which demonstrates that the ZFS is a highly sensitive SH parameter that is very difficult to calculate accurately, especially if only one geometry is considered. The B3LYP/def2-TZVP-calculated D-values, with the coupled perturbed method (CP)[66] method, are 5- to 9-fold smaller than the experimental ones. Hence, this methodology is strongly limited in its predictive ability in this class of complexes. Furthermore, the prediction of the sign of D is wrong even for nearly axial complexes ($E/D \sim 0$), such as $^{\mathrm{H}}$**3** (Table 2).

Table 2. Experimental and Computed ZFS (cm^{-1}) Values, As Well As Decomposition of the Latter in SOC and SSC Contributions, Derived by the Linear Response DFT Couple Perturbed (CP) B3LYP/def2-TZVP Calculations

	complexes			
	1[40]	**2**[40]	**3**[18]	**4**[18]
D^{exp}	~ 6.2	~ −70	−11.9	−12.8
E/D^{exp}	0.3	<0.09	0.02	0.32
	models			
	$^{\mathrm{Me}}$**1**	$^{\mathrm{H}}$**2**	$^{\mathrm{H}}$**3**	$^{\mathrm{H}}$**4**
Co-spin population	2.41	2.38	2.37	2.40
D^{cal}	1.61	8.92	8.21	−3.88
E/D^{cal}	0.01	0.0	0.02	0.21
D^{SOC}	1.33	8.94	9.69	−3.33
$\alpha \rightarrow \alpha$	−0.04	5.07	6.19	−0.38
$\beta \rightarrow \beta$	0.75	0.69	3.39	−2.58
$\alpha \rightarrow \beta$	0.62	3.28	0.24	−0.51
$\beta \rightarrow \alpha$	−0.01	−0.10	−0.13	0.15
D^{SSC}	0.27	−0.01	−1.48	−0.60

Nevertheless, in terms of the individual SOC contributions to D, the results of this investigation show that the spin-conserving transitions ($\alpha \rightarrow \alpha$, $\beta \rightarrow \beta$), as well as the spin-flip transitions ($\alpha \rightarrow \beta$), are the most significant. In any case, it is apparent that no systematic trend can be deduced from the DFT results.

In general, multiconfigurational ab initio calculations are more suitable in the presence of near orbital degeneracy than DFT methods because they can represent all magnetic sublevels explicitly and on an equal footing.[84] Such a treatment, in combination with QDPT, provides a suitable method to treat problems of the kind met here. In the QDPT approach, the SOC (and SS) effects are treated through diagonalization of the SOC (and SS) operators, on the basis of the quartet and doublet roots obtained from SA-CASSCF(7,5), MRDDCI(7,5), or SORCI(7,5) calculations (Table 3). Through the diagonalization, the quartet and doublet states are treated to infinite order in the SOC. We can, therefore, extract the ZFS parameters D and E by using the exact solution of the $S = 3/2$ SH problem for the ZFS.[49] Of course, CASSCF is not an accurate method in the presence of the highly Co−S covalent bonds. However, in correlated ab initio MR-DDCI or SORCI calculations employed on top of the CASSCF wave functions, this shortcoming is considerably reduced, and therefore realistic ZFS predictions should be achievable. This is indeed observed in the Loewdin Co-spin populations presented in Tables 2 and 3. Although the SA-CASSCF calculations predict rather ionic Co−S bonds, with localization of the spin density mainly on the metal center, the MR-DDCI and, to an even larger extent, the SORCI calculations recover the Co−S covalency to levels comparable with the DFT/BP86 calculations.

The D-parameters calculated for the models $^{\mathrm{H}}$**1**, $^{\mathrm{H}}$**2**, $^{\mathrm{H}}$**3**, and $^{\mathrm{H}}$**4** are in satisfactory qualitative agreement with the available experimental data on the corresponding $Co^{(II)}$ complexes (Tables 2 and 3). As is already clear from the SA-CASSCF calculations, the SS contribution to the ZFS is only ~1 cm^{-1} in all the above cases and therefore the magnitude of D is essentially fully determined by SOC contributions.

For $^{\mathrm{H}}$**1**, the calculated large and positive values of D, as well as an $E/D = 0$, are considered unrealistic based on the experimental findings, which are in agreement with large rhombicity ($E/D = 1/3$). To shed more light on this subject, a set of calculations was performed for $^{\mathrm{Me}}$**1**, which are essentially in agreement with experiment (SORCI reference in Table 1). According to these calculations, the major SOC contribution to D arises from the lowest $^4A_2 \rightarrow {}^4E^{xy}$ ($^4T_2^{xy}$) ($d_{x^2-y^2} \rightarrow d_{xz,yz}$) single electron excitations. The splitting of these states reflects a tetragonal compression along the S_4 symmetry axis (Figure 2).

The $^{\mathrm{H}}$**2** and $^{\mathrm{H}}$**3** models correspond to tetrahedral geometries elongated along the four-fold symmetry axis, with negligible rhombic splitting ($E/D = 0$). The main contribution to the ZFS arises from the lowest $^4A_2 \rightarrow {}^4B^z$ ($^4T_2^z$) ($d_{x^2-y^2} \rightarrow d_{xy}$) single electron excitation (Figure 2). For $^{\mathrm{H}}$**2**, the excitation energy to this state is only ~954 cm^{-1}, thus raising D to the enormous value of ~ −89 cm^{-1} in the SORCI reference calculation. Clearly, such an extreme D value is outside the regime within which PT is expected to be valid. Therefore the QDPT treatment is required.

Finally, for $^{\mathrm{H}}$**4**, a negative value of D is predicted by the three methods. However, because of the experimental (and calculated) high rhombicity (E/D~1/3) the sign of D is uncertain. The absolute value of D appears to be overestimated by about 40% compared to experiment (Tables 2, 3). The main SOC contribution to the ZFS is due to the $^4A_2 \rightarrow {}^4A^z$ ($^4T_2^z$) ($d_{x^2-y^2} \rightarrow d_{xy}$), $^4A_2 \rightarrow {}^4E^x$ ($^4T_2^x$) ($d_{x^2-y^2} \rightarrow d_{xz}$), and $^4A_2 \rightarrow {}^4E^y$ ($^4T_2^y$) ($d_{x^2-y^2} \rightarrow d_{yz}$) single electron excitations (Figure 2).

It is apparent from Table 3 that the QDPT method reproduces the experimentally determined ZFS values within <10% of experiment for all studied models. Clearly, second order PT does not have this type of accuracy in the presence of near orbital degeneracy.

g-Tensor. The DFT-calculated **g**-tensors for the $^{\mathrm{Me}}$**1**, $^{\mathrm{H}}$**2**, $^{\mathrm{H}}$**3**, and $^{\mathrm{H}}$**4** models reveal small positive shifts, Δg ~ 0.1−0.2, with respect to the free electron value. These values are underestimated by a factor of ~2 in comparison with the available experimental data. This is quite common for the DFT methods employed here. The g-values are only influenced by spin-allowed (spin-conserving) transitions, and in accordance with the expectations from the LFT[53] they are mainly dominated by the spin conserving $^4A_2 \rightarrow {}^4E^x$ ($d_{x^2-y^2} \rightarrow d_{xz}$), $^4A_2 \rightarrow {}^4E^y$ ($d_{x^2-y^2} \rightarrow d_{yz}$), and $^4A_2 \rightarrow {}^4A^z$ (or $^4B^z$) ($d_{x^2-y^2} \rightarrow d_{xy}$) single electron excitations. The largest positive g-shift is calculated for the g_z parameter of the axial $^{\mathrm{H}}$**2** and $^{\mathrm{H}}$**3** models, in line with experimental observations, owing to the strong SOC effect of the excited $^4B^z$ ($^4T_2^z$) on the $^4A_2$ ground state (Figure 2).

More useful information can be extracted from the calculation of the QDPT effective **g**′-tensors, as they preserve a diagnostic tool of the ground state Kramers doublet ($|\pm 1/2\rangle$ or $|\pm 3/2\rangle$) and thus the sign of D. The **g**′-tensors were calculated by CAS-CI, DDCI2, and SORCI multireference methods. In general, even the "entry level" CAS-CI calculations are able to reproduce the experimental EPR parameters in a fairly satisfactory way. For the axial systems $^{\mathrm{H}}$**2** and $^{\mathrm{H}}$**3**, the **g**′ effective tensors originate from the $|\pm 3/2\rangle$ Kramers doublet, reflecting the expectations for a system with an effective $S = 1/2$ SH.[85] In the case of the S_4 $^{\mathrm{Me}}$**1** model, the introduction of rhombicity allows the mixing of the doublets in a way that $g'_z|\pm 3/2\rangle \sim g'_y|\pm 1/2\rangle$ and vice versa, while $g'_y|\pm 1/2\rangle \sim 3/2 \times g'_y|\pm 3/2\rangle$ (Table 4). Thus, the experimental g' values originate from the $|\pm 1/2\rangle$ Kramers doublet, reflecting the positive sign of D. Upon further lowering of symmetry toward the C_2 $^{\mathrm{H}}$**4** model, significant mixing of the doublets leaves the sign of D still undetermined.

Hyperfine and Ligand Super-Hyperfine A-Tensors. The HFC $A^{Co}_{i,\ i=x,y,z}$ contains three contributions accounting for the

Table 3. Computed ZFS (cm^{-1}) Values and SOC Contributions to D, Derived by CAS-CI, DDCI2, and SORCI Methods

		CAS-CI		DDCI2		SORCI	
model	state	energy	contr. to D	energy	contr. to D	energy	contr. to D
$^{\mathrm{Me}}\mathbf{1}$	$\vert{}^4E^x\rangle$	2973	−12.8	3722	−1.1	3875	−8.2
	$\vert{}^4E^y\rangle$	3050	19.4	3892	14.1	4111	12.8
	$\vert{}^4A^z\rangle$	3294	−6.4	4128	−12.7	4351	−4.3
	$\vert{}^2B^z\rangle$	21794	−3.0	21159	−3.7	19398	−3.3
	$\vert{}^2E^x\rangle$	21851	5.7	21289	6.8	19724	4.1
	$\vert{}^2E^y\rangle$	21863	−2.7	21512	−3.2	20732	−0.5
2nd order PT	D^{SOC}		8.6		6.4		6.2
QDPT	$\vert D^{\mathrm{SOC}}\vert$		7.2		5.7		5.8
	E/D^{SOC}		0.26		0.31		0.31
Co-spin population			2.89		2.85		2.79
$^{\mathrm{H}}\mathbf{2}$	$\vert{}^4B^z\rangle$	822	69.3	969	52.4	954	40.6
	$\vert{}^4E^x\rangle$	3465	15.9	4359	11.4	4771	7.8
	$\vert{}^4E^y\rangle$	3466	−31.2	4362	−21.9	4771	−13.9
	$\vert{}^2B^z\rangle$	20497	−3.1	18722	−3.6	18867	−2.9
	$\vert{}^4E^x\rangle$	21762	−1.1	19749	−1.4	20983	−1.9
	$\vert{}^4E^y\rangle$	21763	3.4	22094	3.9	21534	3.8
2nd order PT	D^{SOC}		−110.11		−87.6		−89.1
QDPT	D^{SOC}		−69.4		−62.8		−64.7
	E/D^{SOC}		0.0		0.0		0.0
Co-spin population			2.88		2.86		2.78
$^{\mathrm{H}}\mathbf{3}$	$\vert{}^4B^z\rangle$	2060	−23.5	2494	−16.5	2438	−18.7
	$\vert{}^4E^x\rangle$	3126	4.8	4018	2.5	4139	3.5
	$\vert{}^4E^y\rangle$	3279	11.2	4198	8.3	4421	7.3
	$\vert{}^2B^z\rangle$	21168	3.1	20146	3.6	20013	4.6
	$\vert{}^2E^x\rangle$	21610	−1.1	21151	−1.0	20095	−2.7
	$\vert{}^2E^y\rangle$	21660	−1.4	21185	−1.8	20131	−0.6
2nd order PT	D^{SOC}		−21.0		−17.4		−18.7
QDPT	D^{SOC}		−16.5		−15.0		−16.4
	E/D^{SOC}		0.04		0.03		0.04
Co-spin population			2.88		2.85		2.77
$^{\mathrm{H}}\mathbf{4}$	$\vert{}^4A^z\rangle$	2700	−52.7	3250	−40.0	3220	−39.2
	$\vert{}^4E^x\rangle$	3070	19.1	3710	14.3	3830	13.4
	$\vert{}^4E^y\rangle$	3420	13.0	4120	9.7	4310	9.0
	$\vert{}^2E^x\rangle$	19800	−3.3	18470	−4.2	19350	−4.1
	$\vert{}^2A^z\rangle$	21100	4.3	19270	5.0	19660	5.1
	$\vert{}^2E^y\rangle$	22700	−2.7	20460	−3.3	20080	−3.0
2nd order PT	D^{SOC}		−20.5		−18.4		−19
QDPT	$\vert D^{\mathrm{SOC}}\vert$		16.4		17.9		17.3
	E/D^{SOC}		0.29		0.30		0.30
Co-spin population			2.88		2.86		2.78

isotropic part A_{iso} (including the Fermi term and pseudo-contact shift, A^{FC}) and the anisotropic A_i part, accounting for the dipolar term SD, $A^{SD}{}_i$, as well the second order SOC contribution $A^{SOC}{}_i$. To a first approximation, LFT[53] provides again qualitative insight into the nature of HFC in high spin, $S = 3/2$, $\mathrm{Co}^{(\mathrm{II})}$ complexes. The HFCs will be dominated by the Fermi contact term and the SD term. The latter is the result of the non-spherical electron distribution around the $\mathrm{Co}^{(\mathrm{II})}$ metal center and the anisotropic

Table 4. Calculated Effective g' Values by CAS-CI, DDCI2 and SORCI Methods for $^{\mathrm{H}}$**4**

		doublet	g'_y	g'_x	g'_z	$\lvert E/D\rvert$
1[38,39]	exp	$\lvert\pm 1/2\rangle$	**5.68**	**2.34**	**1.64**	**0.31**
$^{\mathrm{Me}}$**1**	CAS-CI	$\lvert\pm 1/2\rangle$	6.24	3.01	1.97	0.28
		$\lvert\pm 3/2\rangle$	1.41	1.72	6.62	
	DDCI2	$\lvert\pm 1/2\rangle$	6.15	2.64	1.80	0.30
		$\lvert\pm 3/2\rangle$	1.50	1.92	6.31	
	SORCI	$\lvert\pm 1/2\rangle$	6.04	2.71	1.83	0.32
		$\lvert\pm 3/2\rangle$	1.44	1.82	6.29	
2[38,39]	exp	$\lvert\pm 3/2\rangle$	**<0.6**	**<1.2**	**7.75**	**<0.09**
$^{\mathrm{H}}$**2**	CAS-CI	$\lvert\pm 3/2\rangle$	0.00	0.00	8.95	0.01
		$\lvert\pm 1/2\rangle$	4.35	4.35	3.44	
	DDCI2	$\lvert\pm 3/2\rangle$	0.01	0.02	8.65	0.01
		$\lvert\pm 1/2\rangle$	4.29	4.29	3.2	
	SORCI	$\lvert\pm 3/2\rangle$	0.01	0.01	8.77	0.01
		$\lvert\pm 1/2\rangle$	4.20	4.20	3.30	
3[18,37]	exp	$\lvert\pm 3/2\rangle$	**0.30**	**1.30**	**7.10**	**0.05**
$^{\mathrm{H}}$**3**	CAS-CI	$\lvert\pm 3/2\rangle$	0.31	0.31	7.61	0.04
		$\lvert\pm 1/2\rangle$	4.96	4.37	2.57	
	DDCI2	$\lvert\pm 3/2\rangle$	0.24	0.24	7.30	0.03
		$\lvert\pm 1/2\rangle$	4.72	4.26	2.45	
	SORCI	$\lvert\pm 3/2\rangle$	0.18	0.18	7.28	0.03
		$\lvert\pm 1/2\rangle$	4.64	4.30	2.64	
4[18,37]	exp		**2.68**	**1.62/6.44**	**6.44/1.62**	**0.33**
$^{\mathrm{H}}$**4**	CAS-CI	$\lvert\pm 3/2\rangle$	2.67	1.76	6.81	0.30
		$\lvert\pm 1/2\rangle$	2.12	6.25	1.73	
	DDCI2	$\lvert\pm 3/2\rangle$	2.45	1.66	6.53	0.32
		$\lvert\pm 1/2\rangle$	2.16	6.03	1.70	
	SORCI	$\lvert\pm 3/2\rangle$	2.25	1.56	6.58	0.32
		$\lvert\pm 1/2\rangle$	2.30	5.89	1.78	

covalency, ($\alpha_{xz} \neq \alpha_{yz} \neq \alpha_{xy}$), in the CoS_4 core. The SOC is introduced as in the case of the **g**-tensor, because of the interaction of the excited states with the $^4A_2$ ground state provided by the $^4A_2 \rightarrow {}^4E^x$ ($d_{x^2-y^2} \rightarrow d_{xz}$), $^4A_2 \rightarrow {}^4E^y$ ($d_{x^2-y^2} \rightarrow d_{yz}$), and $^4A_2 \rightarrow {}^4A^z$ ($d_{x^2-y^2} \rightarrow d_{xy}$) spin-conserving single electron excitations.

DFT methods have been successfully used for the calculation of the HFCs in radical systems of small size, as well as for a variety of transition metal complexes. The classic GGA and hybrid-GGA DFT functionals, as well as modern density functionals such as meta-GGA[86] and double hybrid functionals (DHDFs)[72] have been employed to predict experimental HFCs.[67,73a,87] These studies have shown that in DFT there is no general functional for the accurate prediction of transition metal HFCs. The good performance of the TPSSh functional for predicting metal-HFCs was recently pointed out.[73a] For the Co$^{(II)}$ complexes studied in this work, accurate HFCs corresponding to the metal hyperfine ^{59}Co, as well as the ligand super-hyperfine ^{31}P interactions, were obtained for complex **4**.

The principal axes system of the hyperfine **A**-tensors is indicated by (x'', y'', z''). In agreement with the experiment, the principal axis y'' of the metal **A**-tensor was chosen to coincide with the principal axis y' of the effective **g**$'$-tensor, where y' is parallel to the C_2 symmetry axis ($y'//C_2$) (Figure 1). The calculated diagonalized **A**-tensor for model $^{\mathrm{H}}$**4** is in excellent agreement with the corresponding experimental one. In fact, the calculated axes system (x'', y'', z'') of the **A**-tensor, represented by their direction cosines of the principal axes in the molecular axis system in which the effective **g**$'$-tensor is diagonal (x', y', z'), matches the experimental values very well, as illustrated in Figure 3. We can, therefore, assign the experimental **A**-tensor $A_{x''}$, $A_{y''}$, and $A_{z''}$ components as A^{Co}_x, A^{Co}_y, and A^{Co}_z. Table 5 summarizes the calculated metal hyperfine and ligand super-hyperfine coupling constants for $^{\mathrm{H}}$**4**, corresponding to hyperfine interactions on the Co and P_{1-4} atoms, respectively. For the ^{59}Co HFCs, the calculated eigenvalues are acceptable. However, it appears that there is no clear preference among the functionals used. The situation is somewhat more clear-cut for the ^{31}P HFCs, where the hybrid functionals present clear improvements over the GGA functionals. Inspection of the HFC parameters reveals that TPSS is more successful than BP86. More importantly, the hybrid variant TPSSh is significantly superior to TPSS and of similar quality as the widely used B3LYP or PBE0 functionals. The general success of TPSSh to accurately predict HFCs has been recently confirmed in other systems.[73]

$$\begin{bmatrix} & x'' & y'' & z'' \\ x' & -0.873 & 0 & -0.488 \\ y' & 0 & -1 & 0 \\ z' & 0.488 & 0 & -0.873 \end{bmatrix} \quad \begin{bmatrix} & x'' & y'' & z'' \\ x' & -0.848 & 0.000 & -0.529 \\ y' & 0 & -1 & 0 \\ z' & 0.563 & 0.002 & -0.848 \end{bmatrix}$$

Figure 3. Orientation of the principal axes (x'', y'', z'') of the **A**-tensor is represented by their direction cosines in the axes system (x', y', z') of the effective **g**-tensor. Left: ^{59}Co **A**-tensor for **4**, the direction cosines presented here are the result of a later refinement of the data analysis. Right: Calculated TPSSh/CP(PPP)/TZVP ^{59}Co **A**-tensor for $^{\mathrm{H}}$**4**.

Furthermore, the analysis of the **A**-tensor in individual contributions shows that the major part originates from the negative isotropic Fermi contact term and the positive but much smaller SOC contribution. The anisotropy is due to anisotropic covalencies and is reflected in the SD term, which ranges between ∼−30, ∼5, and ∼+30 MHz for A_x, A_y, and A_z, respectively (Table 5).

SH Parameters and Interconversion Pathways. In the above sections, we have dealt with the SH problem statically, by employing carefully designed truncated models, to approximate real structures and to reproduce the experimentally derived SH parameters. However, the SH parameters depend strongly on the symmetry around the Co$^{(II)}$$S_4$ core, a fact requiring the construction of the $D_{2d}(1) \rightarrow S_4 \rightarrow D_{2d}(2)$ (for $^{\mathrm{Me}}$**1** and $^{\mathrm{Me}}$**2**) and the $D_{2d}(1) \rightarrow C_2$ (for $^{\mathrm{H}}$**3** and $^{\mathrm{H}}$**4**) quantum chemical interconversion pathways respectively and, subsequently, the investigation of the variation of the SH parameters along them. Furthermore, the truncated models were fully optimized along the corresponding torsion angle-dependent symmetry interconversion pathways, by employing the same DFT methods, as described above. In this way, one hopes to incorporate the steric and electronic effects of the bulkier groups into the ab initio calculations without facing the prohibitive costs of the calculations on the full systems.

Bonding. Along the $D_{2d}(1) \rightarrow S_4 \rightarrow D_{2d}(2)$ interconversion pathway, the $z//S_4$ axis is retained, while the CoS_4 core is converted from an elongated to compressed structures, as is also reflected in the ground state electron configurations (Figures 1 and 2). Along the $D_{2d}(1) \rightarrow C_2$ interconversion pathway, the $z//S_4$ axis is also retained, but only approximately, as lowering of symmetry from 4-fold to 2-fold occurs. In C_2 symmetry, the N atoms of the two chelating ligands and the Co center are not aligned linearly, as it is the case in $D_{2d}(1,2)$ and S_4 symmetries. Such a distortion renders d_{xy} as effectively non-bonding, decreasing its energy, whereas the energy of d_{xz} and d_{yz} increases, as they are involved

Table 5. Calculated ^{59}Co Hyperfine and Ligand ^{31}P Super-Hyperfine Coupling Constants (MHz) for $^{\mathrm{H}}$**4**

$^{\mathrm{H}}$**4**		B3LYP	BP86	PBE0	TPSS	TPSS0	TPSSh	B2PLYP	exp.[18,37]
Co	$A^{Co}{}_{x}$	−59.6	−16.2	−57.7	−35.9	−86.2	−57.9	−71.4	$A_{x''} = \|118\|$
	A^{FC}	−132.5	−112.4	−175.9	−106.8	−166.8	−132.2	−213.0	
	$A^{SD}{}_{x}$	27.3	33.6	30.2	29.0	25.6	27.7	25.2	
	$A^{SOC}{}_{x}$	45.6	62.6	87.9	41.8	55.0	46.5	116.3	
	$A^{Co}{}_{y}$	−88.0	−49.3	−95.9	−64.1	−115.3	−86.9	−110.4	$A_{y''} = \|45\|$
	A^{FC}	−132.5	−112.4	−175.9	−106.8	−166.8	−132.2	−213.0	
	$A^{SD}{}_{y}$	4.6	11.6	5.2	6.4	2.7	4.5	2.4	
	$A^{SOC}{}_{y}$	39.8	51.4	74.6	36.3	48.7	40.7	100.1	
	$A^{Co}{}_{z}$	−130.1	−115.1	−151.6	−111.1	−153.8	−129.7	−161.8	$A_{z''} = \|107\|$
	A^{FC}	−132.5	−112.4	−175.9	−106.8	−166.8	−132.2	−213.0	
	$A^{SD}{}_{z}$	−31.9	−45.2	−35.5	−35.4	−28.3	−32.2	−27.7	
	$A^{SOC}{}_{z}$	34.4	42.5	59.8	31.2	41.4	34.8	78.9	
$P_{1,3}$	$A_{iso}{}^{FC}$	−1.03	−4.33	−1.03	−1.62	−0.29	−1.43	−0.29	−1.13
$P_{2,4}$	$A_{iso}{}^{FC}$	2.96	2.85	2.51	4.45	2.92	3.15	2.00	1.88

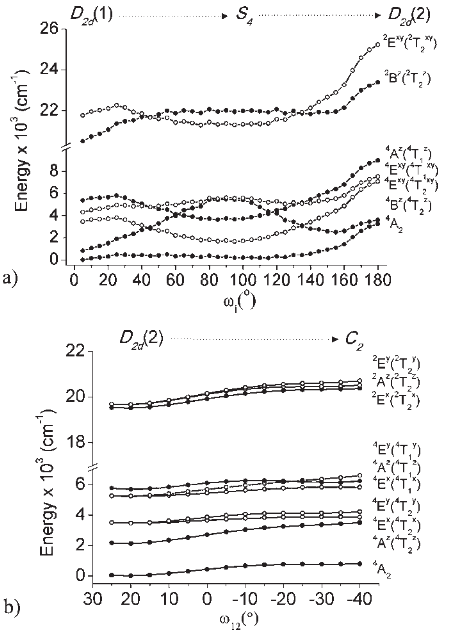

Figure 4. Ground, $^4A_2$, and the lowest excited SOC states, $^{4,2}T_2$, as a function of the torsion angle ω_i, (a) along the $D_{2d}(1) \rightarrow S_4 \rightarrow D_{2d}(2)$, interconversion pathway and (b) along the $D_{2d}(2) \rightarrow C_2$, $\omega_i = \omega_{12}(\omega_{34})$ interconversion pathway.

in Co−S covalent interactions with the ligand S-3p orbitals (Figure 2). The strength of the Co−S bond is provided by the face-alignment of the S-3p orbitals with respect to the Co-d_{xz} and Co-d_{yz} or Co-d_{xy} orbitals. As both D_{2d} and S_4 symmetries require the torsion angles $\omega_{1,2} = \omega_{3,4}$ relation to hold (Scheme 1), covalent Co−S bonds of equal strength result. Furthermore, the C_2 symmetry requires, the torsion angles $\omega_{1,3} < \omega_{2,4}$ relation to hold (Scheme 1). The Co−S bond is strengthened for Co−S−$P_{2,4}$ whereas it is weakened for Co−S−$P_{1,3}$, respectively, along the $D_{2d}(2) \rightarrow C_2$ interconversion pathway. These arguments are in line with the X-ray crystallographic and BP86-calculated bond lengths and BP86 Meyer bond orders, presented in Table 1.

D-Tensor. The SA-CASSCF level interconversion pathways $D_{2d}(1) \rightarrow S_4 \rightarrow D_{2d}(2)$ and $D_{2d}(1) \rightarrow C_2$, between the models $^{\mathrm{H/Me}}$**1** and $^{\mathrm{H/Me}}$**2**, and $^{\mathrm{H}}$**3** and $^{\mathrm{H}}$**4**, respectively, show a strong dependence on the torsion angle ω_i. The former pathway has been constructed by Hirota et al. empirically for complexes **1** and **2**, by employing the angular overlap model (AOM) method, in an effort to explain the origin of the ZFS.[40] However, in the work presented herein, such an approach is performed in a more elaborate way, at the ab initio level, in which the 10 quartet and the 35 doublet states are treated simultaneously. The dependence of the $^4A_2$, $^4E^{xy}$ ($^4T_2{}^{xy}$), $^4B^z$ ($^4T_2{}^z$),$^4E^{xy}$ ($^4T_1{}^{xy}$), and $^4A^z$ ($^4T_1{}^z$) states (of the ^4F term), as well as the corresponding $^2E^{xy}$ ($^2T_2{}^{xy}$) and $^2B^z$ ($^2T_2{}^z$) states (of the ^2G term), on the torsion angle ω_i is presented in Figure 4a. This dependence shows a qualitative picture of the structures involved in the pathway. In fact, at torsion angles $\omega_{12} = 45°$ and 135°, the [Co(SH)$_4$] unit assumes T_d geometry, which requires $D = 0$. For torsion angles $\omega_{12} < 45°$ and $\omega_{12} > 135°$, the $^{2,4}E^{xy}$ ($^{2,4}T_2{}^{xy}$) states are energetically lower than the $^{2,4}B^z$($^{2,4}T_2{}^z$) states, whereas for torsion angles $45° < \omega_{12} < 135°$ the order of the levels reverses. The orbital splitting follows the same trend; thus for torsion angles $\omega < 45°$ and $\omega > 135°$, the [CoSH$_4$] is elongated along the four-fold symmetry axis and therefore the energy of d_{xy} decreases, whereas the energy of $d_{xz,yz}$ increases. By contrast, for torsion angles $45° < \omega < 135°$, the reverse is observed (Figure 5). For the $D_{2d}(1)$, $\omega_i = 0°$ and $D_{2d}(2)$ $\omega_i = 180°$ geometries, the main SOC contribution to the ZFS arises from the $^4A_2 \rightarrow {}^4B^z$ ($d_{x^2-y^2} \rightarrow d_{xy}$) single electron excitation within the $^4T_2$ states, while for the S_4 geometries, $\omega_{12} \sim 90°$, the SOC contributions to the ZFS involve the $^4A_2 \rightarrow {}^4E^{xy}$ ($d_{x^2-y^2} \rightarrow d_{xy,yz}$) single electron excitations, as can be seen in Figure 4a. Furthermore, the calculated CAS-CI ZFS values, by both PT and QDPT calculations of the energy separation between the $|\pm 1/2\rangle$ and $|\pm 3/2\rangle$ Kramers doublets (Figure 6a), shows that D_{2d} geometries are characterized by negative D values, and the corresponding S_4 geometries by positive D values. However, only in the narrow region of $-10 < D < +10$ cm^{-1}, the second order PT curve is collinear with the QDPT curve, an observation showing that outside this region, the PT approach essentially breaks down. This is not, for instance, the case for octahedral Cr$^{(II)}$ and Cr$^{(III)}$ hexaaquo complexes,[42] for which the second order perturbation approach is fully adequate for the calculation of the **D**-tensor. Clearly these two SOC contributions are responsible for the break down of the PT approach, as shown in Figure 4a. In the region of torsion angles $45° < \omega_i < 135°$ dominated by S_4 CoS$_4$ cores, E/D varies between 0 and 0.25, a

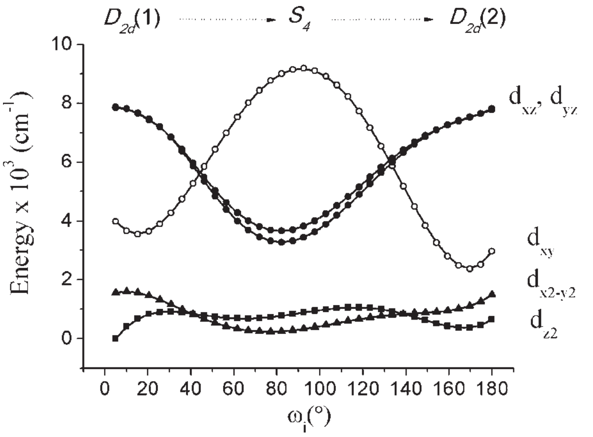

Figure 5. d-Orbital splitting along the $D_{2d}(1)\rightarrow S_4\rightarrow D_{2d}(2)$ interconversion pathway, as a function of the torsion angle ω_i.

fact associated with the $d_{xz,yz}$ orbital splitting, as well as with the splitting of the $^4E^{xy}$ ($^4T_2^{xy}$) lowest excited state (Figure 4a, 5).

As extensively discussed above, in the case of **4**, further reduction of the symmetry toward C_2, leaves the sign of D undetermined, both experimentally and by ab initio theoretical methods applied over static geometries. However, the condition which reverses the sign of D along the $D_{2d}(1)\rightarrow S_4\rightarrow D_{2d}(2)$ interconversion pathway is not satisfied along the corresponding $D_{2d}(1)\rightarrow C_2$ interconversion pathway for $^{\mathrm{H}}$**3** and $^{\mathrm{H}}$**4** models, respectively, as the $\mathrm{Co^{(II)}S_4}$ core effectively avoids the $\sim T_d$ symmetry ($D = 0$). On the other hand, the negative value of D calculated at the initial $D_{2d}(1)$ point of the pathway ($\omega_{12} = \omega_{34} = 25°$) increases linearly toward a maximum at $\omega_{12} = \omega_{34} = -30°$ and then decreases at $\omega_{12} = \omega_{34} = -45°$ ($\sim C_2$ symmetry), where the **D**-tensor reaches its maximum rhombicity ($E/D\sim 0.3$) (Figure 6b). As a result of extreme rhombicity, the e($d_{xz,yz}$) orbitals split along the $D_{2d}(2)\rightarrow C_2$ pathway, as in the case of the $D_{2d}(1)\rightarrow S_4\rightarrow D_{2d}(2)$ interconversion pathway. However, the final electron configuration $d_{x^2-y^2}^{\;2} d_{z^2}^{\;2} d_{xy}^{\;1} d_{yz}^{\;1} d_{xz}^{\;1}$ (Figure 2) does not reverse the splitting of the $^4T_2$ ($^4A^z$ and $^4E^{xy}$) states (Figure 4b), retaining the sign of D negative. It is remarkable that a very similar behavior in the orbital splitting of $^{\mathrm{H}}$**4** with respect to $^{\mathrm{H}}$**2** and $[\mathrm{Co(PPh)_3Cl_2}]$[44] is observed, which accounts for the negative sign of D in these cases. In addition, the plot of the QDPT versus PT curves for the ZFS do not coincide, because of strong SOC effects between the $^4A^z$ excited state with the $^4A_2$ ground state, in analogy with the $^{\mathrm{H/Me}}$**1** and $^{\mathrm{H/Me}}$**2** model complexes around $D_{2d}(1)$ symmetry (Figure 6b). We therefore, conclude that second order PT methods in general are not adequate for describing the ZFS of $S = 3/2$ $\mathrm{Co^{(II)}S_4}$ complexes.

In summary, the CAS-CI-constructed $D_{2d}(1)\rightarrow S_4\rightarrow D_{2d}(2)$ and $D_{2d}(1)\rightarrow C_2$ pathways explain the experimental magnetic properties of $\mathrm{Co^{(II)}S_4}$ complexes in terms of LFT. These results are superior to the previously applied AOM approach, as the ab initio method is quantitatively and qualitatively more correct and does not contain adjustable parameters. As discussed in the previous sections, inclusion of dynamic correlation offers even more reliable values for the ZFS parameters.

g-Tensor. The effective $\mathbf{g}'$-tensors calculated by QDPT present a diagnostic tool of the ground state Kramers doublet for D_{2d} and S_4 symmetries, respectively. This is nicely observed along the $D_{2d}(1)\rightarrow S_4\rightarrow D_{2d}(2)$ interconversion pathway, in which well-defined regions can be identified for the $\mathbf{g}'$ tensors for the $|\pm1/2\rangle$ and $|\pm3/2\rangle$ doublets, respectively. According to the expectation from the LFT[53] and the $S' = 1/2$ SH approach toward the $D_{2d}(2)\rightarrow S_4$ pathway, $g'_z|\pm1/2\rangle$ and $g'_z|\pm3/2\rangle$ decrease as the ^4B_z excited state gets lower than the $^4E^{xy}$ state (Figure 7a). Along the same lines, $g'_{xy}|\pm1/2\rangle$ and $g'_{xy}|\pm3/2\rangle$ would equally decrease; however, introduction of rhombicity splits them apart. In D_{2d} and S_4 symmetries, the d_{xy} an $d_{xz,yz}$ orbitals are not allowed to mix and therefore the composition of the $g'_z|\pm3/2\rangle$ and $g'_y|\pm1/2\rangle$ remains pure, even in the presence of extreme rhombicity. Thus, determination of the sign of D by both accurate experimental and theoretical methods is feasible. In addition, around D_{2d} symmetry, the observation of transitions within both Kramers doublets is possible. In fact, for complex **3**, two transitions[18] could be identified at $g' = 7.1$ and $g' = 5.8$, which, according to Figure 7b, can be assigned as $g'_z|\pm3/2\rangle$ and $g'_y|\pm1/2\rangle$ and $g'_x|\pm1/2\rangle$, respectively. Toward C_2 symmetry, significant mixing of the doublets is observed, dividing the spectral region into two groups: the one at $g' \sim 7$, which is dominated by $g'_z|\pm3/2\rangle$ and $g'_y|\pm1/2\rangle$, and a second one ranging between $g' \sim 4$ and $g' \sim 1$, which is dominated by compositions of the remaining effective $\mathbf{g}'$-tensors (Figure 7b).

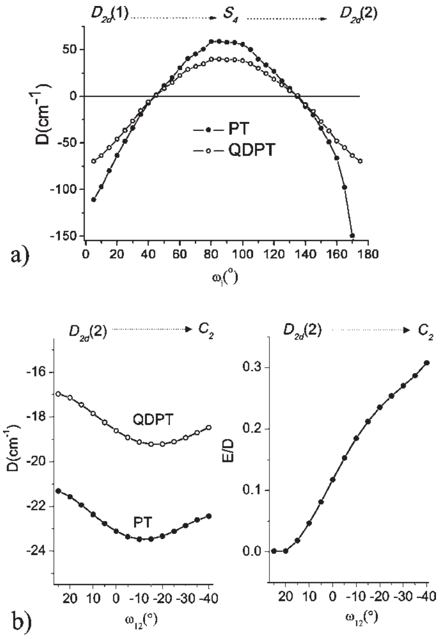

Figure 6. a) Comparison of the QDPT vs PT D values (a) along the $D_{2d}(1)\rightarrow S_4\rightarrow D_{2d}(2)$ interconversion pathway and (b) along the $D_{2d}(2)\rightarrow C_2$ interconversion pathway, as a function of the torsion angle $\omega_i = \omega_{12}(\omega_{34})$ (left). In (b) (right) the rhombicity E/D as a function of the torsion angle $\omega_i = \omega_{12}(\omega_{34})$, along the $D_{2d}(2)\rightarrow C_2$ interconversion pathway, is plotted.

Metal A-Tensor. The calculation of the metal HFCs along the $D_{2d}(2)\rightarrow C_2$ interconversion pathway shows that the anisotropy of HFCs, provided by the SD interaction, is torsion angle dependent. Axial $D_{2d}(2)$ structures possess nearly isotropic HFCs ($A^{Co}_z \sim A^{Co}_{xy}$). Lowering of symmetry toward C_2 introduces large anisotropy in the SD term in which $|A^{SD}_x|$ and $|A^{SD}_y|$ decrease, whereas $|A^{SD}_z|$ increases, along the scan (Figure 8). On the other hand, A^{SOC} shows very small anisotropy ($\Delta A^{SOC} < 6$ MHz), and, in addition, A^{FC} remains essentially constant. Therefore, the main anisotropic contribution to A^{Co}_i along the $D_{2d}(2)\rightarrow C_2$ interconversion pathway, is provided by the SD term.

Following this argument, the d_{xy} orbital becomes non-bonding in C_2 symmetry. Therefore, the Co−S covalent bonding is provided

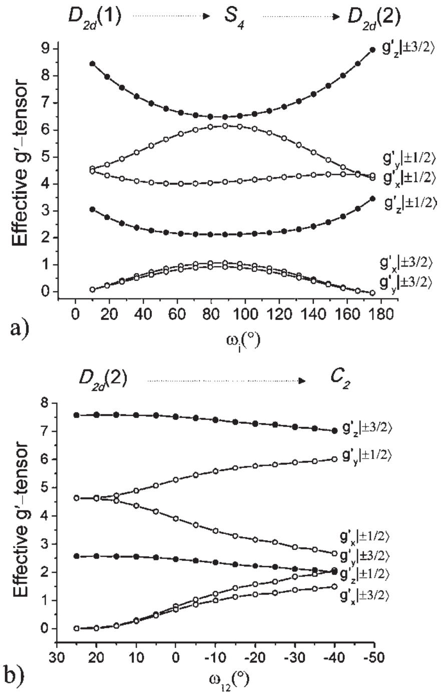

Figure 7. QDPT CASSCF(7,5)-calculated $\mathbf{g}'$ tensors along (a) the $D_{2d}(1)$→S_4→ $D_{2d}(2)$ and (b) $D_{2d}(2)$→C_2 interconversion pathways, as a function of the torsion angles ω_i and $\omega_i = \omega_{12}(\omega_{34})$, respectively.

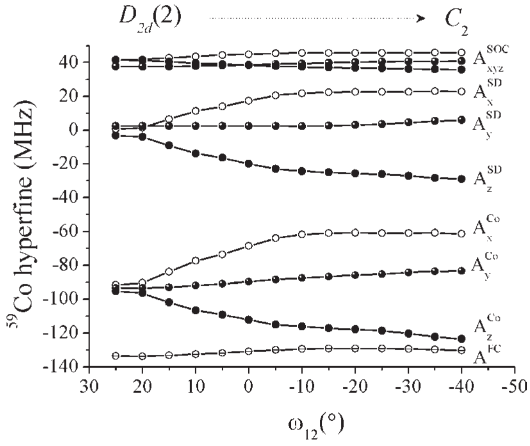

Figure 8. TPSSh/CP(PPP)/TZVP calculation of the ^{59}Co **A**-tensor and its decomposition in FC, SD, and SOC contributions along the $D_{2d}(2)$→C_2 interconversion pathway, as a function of the torsion angle $\omega_i = \omega_{12}(\omega_{34})$ for the $^{\mathbf{H}}$**4** model.

mainly by the interaction of the d_{yz} and d_{xz} orbitals with the S lone pairs. Thus, in accordance with the expectations from the LFT,[53] the calculated $|A^{Co}{}_x|$ and $|A^{Co}{}_y|$ are decreased from 91 MHz, to 58 and 88 MHz, respectively, whereas the $|A^{Co}{}_z|$ is increased from 95 to 127 MHz along the TPSSh $D_{2d}(2)$→C_2 interconversion pathway. Along the same lines, the sign of the isotropic hyperfine interaction on the P atoms is reproduced, confirming that the small s-spin density is negative on the P_{13} and positive on the P_{24} atoms that carry the Ph and the ^{i}Pr groups in the real complex **4**, respectively.[37] Such a trend is consistent with an electron density flow from the P^{i}Pr$_2$ fragment, carrying the electron donating ^{i}Pr groups, to the PPh$_2$ fragment bearing the electron accepting Ph groups, via the central metal atom, corresponding to a significant delocalization of the spin density onto the ligand framework. This proposal is in agreement with ^{31}P NMR data for complex **4**[32] and reflects the covalent nature of the Co−S bonds.

■ CONCLUSIONS

This work provides a systematic computational study of high spin Co$^{(II)}$S$_4$-containing complexes, following their experimental investigation by X-band EPR, HF-EPR, and ENDOR spectroscopy. The ab initio multireference configuration interaction and DFT computational methods were applied to map the electronic structures of these complexes. The magnitude of D was calculated by employing multiconfigurational ab initio methods. The available large experimental window for D in such systems (+6 to −70 cm^{-1}) allows conclusive remarks on the applicability of each method used. Reliable calculated D and E/D values are obtained using QDPT in conjunction with correlated multireference methods (SORCI, MR-DDCI2). In particular, the theoretical investigation of the ZFS for the $^{\mathbf{H/Me}}$**1**, $^{\mathbf{H/Me}}$**2**, $^{\mathbf{H}}$**3**, and $^{\mathbf{H}}$**4** models and the mapping of the ZFS along the relevant symmetry interconversion pathways $D_{2d}(1)$→S_4→ $D_{2d}(2)$ and $D_{2d}(2)$→C_2 indicate that there is only a narrow region, $-10 < D < +10$ cm^{-1}, for which the second order PT is adequate for calculating the ZFS of such systems. The main contribution to the ZFS for the above set of models arises from SOC contributions that couple the $^4T_2$ excited states to the $^4A_2$ ground state.

Apart from the magnitude of D, its sign is an important parameter for an EPR study. It was a great challenge to deal with this important property for the systems under study, as the EPR experiments were not able to resolve the matter under rhombic conditions ($E/D > 0.2$). In that respect, careful appraisal of the investigated electronic structures categorize our model set in two main configurations, namely, $d_{z^2}{}^2 d_{x^2-y^2}{}^2 d_{xy}{}^1 d_{yz}{}^1 d_{xz}{}^1$ and $d_{x^2-y^2}{}^2 d_{z^2}{}^2 d_{yz}{}^1 d_{xz}{}^1 d_{xy}{}^1$, accounting for negative and positive signs of D, respectively. In the special case of $^{\mathbf{H}}$**4**, for which the experiments did not conclusively provide the sign of D, we have included the most important SH components, in terms of effective $\mathbf{g}'$, **D**, and hyperfine coupling **A** tensors in this study. In our treatment, we were careful to follow the experimental principal axis system by performing our calculations for the experimental structures of **3** and **4**. By this procedure, direct comparisons with the experimental matrices could be made. The effective $\mathbf{g}'$ tensors were calculated by applying QDPT methods. The results show substantial differences between the |±1/2⟩ and |±3/2⟩ Kramers doublets, which allows the determination of the sign of D. The results are consistent with the experiment. Interestingly such methodology seems to have wider applications for the theoretical investigation of other half-spin systems, as it was successfully applied for $S = 1/2$ low-spin Mo(III) complexes as well.[88]

In the case of $^{\mathbf{H}}$**4**, the metal hyperfine tensor, $\mathbf{A}^{\mathbf{Co}}{}_{\mathbf{i}}$, and the isotropic ligand super-hyperfine tensor, $\mathbf{A}^{\mathbf{P}}{}_{\mathbf{iso}}$, was systematically studied at the DFT level by employing various functionals. The best results were obtained by the GGA: PBE, hybrid GGA B3LYP and meta GGA: TPSSh functionals, with the latter providing the overall most accurate predictions. These results are in line with previous studies. Decomposition of the $\mathbf{A}^{\mathbf{Co}}$ tensor into its contributions (FC, SD, and SOC) along the $D_{2d}(2)$→C_2 interconversion pathway, in combination with LFT arguments, reveals a variability of the electronic structure on Co$^{R,R'}$L$_2$ complexes. The nature of the R,R' peripheral groups largely affects the electronic properties of such Co$^{(II)}$S$_4$-containing complexes. This observation has wider significance, owing to the presence of such metallic cores in the active sites of cobalt or cobalt-reconstituted proteins. Reinforcing the findings of this work, it has recently been shown that in the case of the corresponding tetrahedral Ni$^{R,R'}$L$_2$ complexes, the covalent character of the Ni−S bonds is increased along the $D_{2d}(2)\rightarrow C_2$ interconversion pathway, leading not only to a different geometry (square-planar) but also to different ground state spin multiplicities.[63]

Overall, the recent experimental work,[18,37] combined with the theoretical work presented herein, provides a basis for further investigation of inorganic and biological Co$^{(II)}$S$_4$-containing systems.

■ AUTHOR INFORMATION

Corresponding Author

*E-mail: kyritsis@chem.uoa.gr (P.K.), neese@thch.uni-bonn.de (F.N.). Phone: +49-228-732351 (F.N.). Fax: +49-228-739064 (F.N.).

■ ACKNOWLEDGMENT

D.M. and F.N. acknowledge financial support from the DFG priority program SFB 813 "Chemistry at Spin centers". P.K. thanks the Special Account of the University of Athens for funding (Grant 7575). We would like also to thank the reviewers for their constructive criticism.

■ ABBREVIATIONS

EPR, electron paramagnetic resonance; MCD, magnetic circular dichroism; ZFS, zero-field splitting; DFT, density functional theory; SH, Spin Hamiltonian; SOC, spin−orbit coupling; SSC, spin−spin coupling; QDPT, quasi-degenerate perturbation theory; CAS-CI, Complete active space configuration interaction; MR-DDCI2, Multi Reference-difference dedicated CI with two degrees of freedom; SORCI, Spectroscopy ORiented CI

■ REFERENCES

(1) Holm, R. H.; Kennepohl, P.; Solomon, E. I. *Chem. Rev.* **1996**, *96*, 2239–2314.

(2) Solomon, E. I. *Inorg. Chem.* **2005**, *44*, 723–726.

(3) Holm, R. H.; Solomon, E. I. *Chem. Rev.* **2004**, *104*, 347–348.

(4) Solomon, E. I.; Randall, D. W.; Glaser, T. *Coord. Chem. Rev.* **2000**, *200*, 595–632.

(5) Solomon, E. I.; Szilagyi, R. K.; George, S. D.; Basumallick, L. *Chem. Rev.* **2004**, *104*, 419–458.

(6) Abragam, A.; Bleaney, B. *Electron Paramagnetic Resonance of Transition Ions*; Dover Publications Inc.: New York, 1986.

(7) Hagen, W. R. *Coord. Chem. Rev.* **1999**, *192*, 209–229.

(8) Krzystek, J.; Zvyagin, S. A.; Ozarowski, A.; Trofimenko, S.; Telser, J. *J. Magn. Reson.* **2006**, *178*, 174–183.

(9) Bŏca, R. *Coord. Chem. Rev.* **2004**, *248*, 757–815.

(10) Duboc, C.; Collomb, M.-N.; Pécaut, J.; Deronzier, A.; Neese, F. *Chem.—Eur. J.* **2008**, *14*, 6498–6509.

(11) Cirera, J.; Ruiz, E.; Alvarez, S.; Neese, F.; Kortus, J. *Chem.—Eur. J.* **2009**, *15*, 4078–4087.

(12) Aromi, G.; Brechin, E. K. *Struct. Bonding (Berlin)* **2006**, *122*, 1–67.

(13) Cornia, A.; Costantino, A. F.; Zobbi, L.; Caneschi, A.; Gatteschi, D.; Mannini, M.; Sessoli, R. *Struct. Bonding (Berlin)* **2006**, *122*, 133–161.

(14) Neese, F.; Pantazis, D. A. *Faraday Discuss.* **2011**, *148*, 229–238.

(15) Murrie, M. *Chem. Soc. Rev.* **2010**, *39*, 1986–1995.

(16) Ostrovsky, S.; Tomkowicz, Z.; Haase, W. *Coord. Chem. Rev.* **2009**, *253*, 2363–2375.

(17) Krzystek, J.; Zvyagin, S. A.; Ozarowski, A.; Fiedler, A. T.; Brunold, T. C.; Telser, J. *J. Am. Chem. Soc.* **2004**, *126*, 2148–2155.

(18) Maganas, D.; Milikisyants, S.; Rijnbeek, J. M. A.; Sottini, S.; Levesanos, N.; Kyritsis, P.; Groenen, E. J. J. *Inorg. Chem.* **2010**, *49*, 595–605.

(19) Krzystek, J.; Ozarowski, A.; Telser, J. *Coord. Chem. Rev.* **2006**, *250*, 2308–2324.

(20) Barra, A. L.; Gatteschi, D.; Sessoli, R.; Sorace, L. *Magn. Reson. Chem.* **2005**, *43*, S183–S191.

(21) Champion, P. M.; Sievers, A. J. *J. Chem. Phys.* **1977**, *66*, 1819–1825.

(22) van Slageren, J.; Vongtragool, S.; Gorshunov, B.; Mukhin, A. A.; Karl, N.; Krzystek, J.; Telser, J.; Muller, A.; Sangregorio, C.; Gatteschi, D.; Dressel, M. *Phys. Chem. Chem. Phys.* **2003**, *5*, 3837–3843.

(23) Vongtragool, S.; Gorshunov, B.; Dressel, M.; Krzystek, J.; Eichhorn, D. M.; Telser, J. *Inorg. Chem.* **2003**, *42*, 1788–1790.

(24) Schnegg, A.; Behrends, J.; Lips, K.; Bittl, R.; Holldack, K. *Phys. Chem. Chem. Phys.* **2009**, *11*, 6820–6825.

(25) Krzystek, J.; Swenson, D. C.; Zvyagin, S. A.; Smirnov, D.; Ozarowski, A.; Telser, J. *J. Am. Chem. Soc.* **2010**, *132*, 5241–5253.

(26) Carrell, C. J.; Wang, X. T.; Jones, L. M.; Jarrett, W. L.; Davidson, V. L.; Mathews, F. S. *Biochemistry* **2004**, *43*, 9381–9389.

(27) Walsby, C. J.; Krepkiy, D.; Petering, D. H.; Hoffman, B. M. *J. Am. Chem. Soc.* **2003**, *125*, 7502–7503.

(28) Johansson, F. B.; Bond, A. D.; Nielsen, U. G.; Moubaraki, B.; Murray, K. S.; Berry, K. J.; Larrabee, J. A.; McKenzie, C. J. *Inorg. Chem.* **2008**, *47*, 5079–5092.

(29) Larrabee, J. A.; Chyun, S. A.; Volwiler, A. S. *Inorg. Chem.* **2008**, *47*, 10499–10508.

(30) Hadler, K. S.; Mitic, N.; Yip, S. H. C.; Gahan, L. R.; Ollis, D. L.; Schenk, G.; Larrabee, J. A. *Inorg. Chem.* **2010**, *49*, 2727–2734.

(31) Gilby, L. M.; Piggott, B. *Polyhedron* **1999**, *18*, 1077–1082.

(32) Maganas, D.; Staniland, S. S.; Grigoropoulos, A.; White, F.; Parsons, S.; Robertson, N.; Kyritsis, P.; Pneumatikakis, G. *Dalton Trans.* **2006**, 2301–2315.

(33) Ly, T. Q.; Woollins, J. D. *Coord. Chem. Rev.* **1998**, *176*, 451–481.

(34) Silvestru, C.; Drake, J. E. *Coord. Chem. Rev.* **2001**, *223*, 117–216.

(35) Haiduc, I. Dichalcogenoimidodiphosphinato Ligands. In *Comprehensive Coordination Chemistry II: From Biology to Nanotechnology*; McCleverty, J. A., Meyer, T. J., Eds.; Elsevier Pergamon: Amsterdam, The Netherlands, 2004; Vol. 1, pp 323−347.

(36) Chivers, T.; Ritch, J. S.; Robertson, S. D.; Konu, J.; Tuononen, H. M. *Acc. Chem. Res.* **2010**, *43*, 1053–1062.

(37) Sottini, S.; Mathies, G.; Gast, P.; Maganas, D.; Kyritsis, P.; Groenen, E. J. J. *Phys. Chem. Chem. Phys.* **2009**, *11*, 6727–6732.

(38) Fukui, K.; Ohyanishiguchi, H.; Hirota, N. *Bull. Chem. Soc. Jpn.* **1991**, *64*, 1205–1212.

(39) Fukui, K.; Kojima, N.; Ohyanishiguchi, H.; Hirota, N. *Inorg. Chem.* **1992**, *31*, 1338–1344.

(40) Fukui, K.; Masuda, H.; Ohyanishiguchi, H.; Kamada, H. *Inorg. Chim. Acta* **1995**, *238*, 73–81.

(41) Neese, F.; Munzarova, M. L. Historical Aspects of EPR Parameter Calculations. In *Calculation of NMR and EPR Parameters*; Kaupp, M., Ed.; Wiley: New York, 2004; pp 21−32.

(42) Liakos, D. G.; Ganyushin, D.; Neese, F. *Inorg. Chem.* **2009**, *48*, 10572–10580.

(43) Neese, F. *J. Am. Chem. Soc.* **2006**, *128*, 10213–10222.

(44) Sundararajan, M.; Ganyushin, D.; Ye, S. F.; Neese, F. *Dalton Trans.* **2009**, 6021–6036.

(45) Pilbrow, J. R. *J. Magn. Reson.* **1978**, *31*, 479–490.

(46) Neese, F. In *Biological Magnetic Resonance*; Hanson, G.; Berliner, L., Eds; Springer: New York, 2009; Vol. 28, pp 175−229.

(47) Zein, S.; Duboc, C.; Lubitz, W.; Neese, F. *Inorg. Chem.* **2007**, *47*, 134–142.

(48) *Principles of electron spin resonance*; Atherton, N. M., Ed; Ellis Horwood; PTR Prentice Hall: New York, 1993.

(49) McWeeny, R. *Methods of Molecular Quantum Mechanics*; Academic: London, 1992.

(50) Neese, F.; Solomon, E. I. *Inorg. Chem.* **1998**, *37*, 6568–6582.

(51) Neese, F. *J. Chem. Phys.* **2005**, *122*, 034107.

(52) Bolvin, H. *Chem. Phys. Chem.* **2006**, *7*, 1575–1589.

(53) Neese, F.; Solomon, E. I. In *Magnetoscience-From Molecules to Materials*; Miller, J. S.; Drillon, M., Eds; Wiley: New York, **2003**; Vol. *IV*, pp 345−466.

(54) Neese, F. *ORCA- an ab initio, density functional and semiempirical program package,* Version 2.6.35; University of Bonn: Bonn, Germany, 2008.

(55) Becke, A. D. *Phys. Rev. A* **1988**, *38*, 3098–3100.

(56) Perdew, J. P. *Phys. Rev. B* **1986**, *33*, 8822–8824.

(57) Becke, A. D. *J. Chem. Phys.* **1993**, *98*, 5648–5652.

(58) Lee, C.; Yang, W.; Parr, R. G. *Phys. Rev. B* **1988**, *37*, 785–789.

(59) (a) Schäfer, A.; Huber, C.; Ahlrichs, R. *J. Chem. Phys.* **1994**, *100*, 5829–5835. (b) Krishnan, R.; Binkley, J. S.; Seeger, R.; Pople, J. A. *J. Chem. Phys.* **1980**, *72*, 650–654.

(60) Hess, B. A. *Phys. Rev. A* **1985**, *32*, 756–763.

(61) Hess, B. A. *Phys. Rev. A* **1986**, *333*, 3742–3748.

(62) Jansen, G.; Hess, B. A. *Phys.Rev. A* **1989**, *39*, 6016–6017.

(63) Maganas, D.; Grigoropoulos, A.; Staniland, S. S.; Chatziefthimiou, S. D.; Harrison, A.; Robertson, N.; Kyritsis, P.; Neese, F. *Inorg. Chem.* **2010**, *49*, 5079–5093.

(64) Weigend, F.; Ahlrichs, R. *Phys. Chem. Chem. Phys.* **2005**, *7*, 3297–3305.

(65) Neese, F. *J. Chem. Phys.* **2003**, *119*, 9428–9443.

(66) Neese, F. *J. Chem. Phys.* 2007, 127, Article number 164112.

(67) Neese, F. *J. Chem. Phys.* **2003**, *118*, 3939–3948.

(68) Adamo, C.; di Matteo, A.; Barone, V. *Adv. Quantum Chem.* **2000**, *36*, 45–75.

(69) Tao, J. M.; Perdew, J. P.; Staroverov, V. N.; Scuseria, G. E. *Phys. Rev. Lett.* **2003**, *91*, 146401.

(70) Staroverov, V. N.; Scuseria, G. E.; Tao, J.; Perdew, J. P. *J. Chem. Phys.* **2003**, *119*, 12129–12137.

(71) A 25% exchange version of TPSSh

(72) Grimme, S. *J. Chem. Phys.* **2006**, *124*, 34108–34123.

(73) (a) Kossmann, S.; Kirchner, B.; Neese, F. *Mol. Phys.* **2007**, *105*, 2049–2071. (b) Pantazis, D. A.; Orio, M.; Petrenko, T.; Zein, S.; Bill, E.; Lubitz, W.; Messinger, J.; Neese, F. *Chem.—Eur. J.* **2009**, *15*, 5108–5123.

(74) Neese, F. *Inorg. Chim. Acta* **2002**, *337*, 181–192.

(75) van Lenthe, E.; van der Avoird, A.; Wormer, P. E. S. *J. Chem. Phys.* **1998**, *108*, 4783–4796.

(76) van Lenthe, E.; Baerends, E. J.; Snijders, J. G. *J. Chem. Phys.* **1993**, *99*, 4597–4610.

(77) Heully, J. L.; Lindgren, I.; Lindroth, E.; Lundquist, S.; Martensson, A. M. *J. Phys. B* **1986**, *19*, 2799–2815.

(78) Otto, J.; Jolk, I.; Viland, T.; Wonnemann, R.; Krebs, B. *Inorg. Chim. Acta* **1999**, *285*, 262–268.

(79) Vrajmasu, V. V.; Bominaar, E. L.; Meyer, J.; Munck, E. *Inorg. Chem.* **2002**, *41*, 6358–6371.

(80) Vrajmasu, V. V.; Munck, E.; Bominaar, E. L. *Inorg. Chem.* **2004**, *43*, 4867–4879.

(81) Neese, F. *J. Inorg. Biol. Chem.* **2006**, *100*, 716–726.

(82) Schöneboom, J. C.; Neese, F.; Thiel, W. *J. Am. Chem. Soc.* **2005**, *127*, 5840–5853.

(83) Ye, S.; Neese, F.; Ozarowski, A.; Smirnov, D.; Krzystek, J.; Telser, J.; Liao, J.-H.; Hung, C.-H; Chu, W.-C.; Tsai, Y.-F.; Wang, R.-C.; Chen, K.-Y.; Hsu, H.-F. *Inorg. Chem.* **2010**, *49*, 977–988.

(84) Neese, F.; Petrenko, T.; Ganyushin, D.; Olbrich, G. *Coord. Chem. Rev.* **2007**, *251*, 288–327.

(85) Banci, L.; Bencini, A.; Benelli, C.; Gatteschi, D.; Zanchini, C. *Struct. Bonding (Berlin)* **1982**, *52*, 37–86.

(86) Perdew, J. P.; Kurth, S.; Zupan, A.; Blaha, P. *Rev. Lett.* **1999**, *82*, 2544–2547.

(87) Remenyi, C.; Reviakine, R.; Arbuznikov, A, V.; Vaara, Y.; Kaupp, M. *J. Phys. Chem. A* **2004**, *108*, 5026–5033.

(88) McNaughton, R. L.; Roemelt, M.; Chin, J. M.; Schrock, R. R.; Neese, F.; Hoffman, B. M. *J. Am. Chem. Soc.* **2010**, *132*, 8645–8656.

(89) There are no crystalographic data for **2**.The structure was taken from the Cambridge Structural Database (code: GUFGOD).